Polycrystalline Plasticity and the Evolution of Crystallographic Texture in FCC Metals

C. A. Bronkhorst, S. R. Kalidindi and L. Anand

Phil. Trans. R. Soc. Lond. A 1992 **341**, 443-477
doi: 10.1098/rsta.1992.0111

Polycrystalline plasticity and the evolution of crystallographic texture in FCC metals

By C. A. Bronkhorst, S. R. Kalidindi and L. Anand

Department of Mechanical Engineering, Massachusetts Institute of Technology,
Cambridge, Massachusetts 02139, U.S.A.

Contents

A Taylor-type model for large deformation polycrystalline plasticity is formulated and evaluated by comparing the predictions for the evolution of crystallographic texture and the stress–strain response in simple compression and tension, plane strain compression, and simple shear of initially 'isotropic' OFHC copper against (*a*) corresponding experiments, and (*b*) finite element simulations of these experiments using a multitude of single crystals with accounting for the satisfaction of both compatibility and equilibrium. Our experiments and calculations show that the Taylor-type model is in reasonable first-order agreement with the experiments for the evolution of texture and the overall stress–strain response of single-phase copper. The results of the finite element calculations are in much better agreement with experiments, but at a substantially higher computational expense.

---

1. Introduction

In polycrystalline metals, the two major causes of anisotropic plastic response are (*a*) crystallographic texture resulting from the reorientation of the crystal lattices of grains during deformation, and (*b*) morphological texture resulting from the nonequiaxed shape of highly deformed grains. There have been considerable recent advances in the understanding of anisotropy due to crystallographic texturing (Gil Sevillano *et al.* 1980; Asaro 1983*a*, *b*; Wenk 1985). Asaro & Needleman (1985) have developed an elastic-plastic, rate-dependent polycrystalline model for low homologous temperatures in which inelastic deformation within the individual crystals is taken to be by crystallographic slip alone. To predict the global response of the

Phil. Trans. R. Soc. Lond. A (1992) **341**, 443–477

Printed in Great Britain

polycrystal, the transition from the micro-response of the individual grains to the macro-response of the polycrystalline aggregate, Asaro & Needleman (1985) follow the pioneering work of Taylor (1938). They assume that all grains have equal volume, and that the deformation gradient within each grain has a uniform value throughout the aggregate. In this approximate model, compatibility is satisfied and equilibrium holds in each grain, but equilibrium is usually violated between grains. This simple averaging procedure gives that the macroscopic average Cauchy stress in the polycrystal is simply the number average of the Cauchy stress in each crystal. In this model, the deformation producing mechanisms of twinning, diffusion and grain boundary sliding are not considered, and other sources of anisotropy due to the morphological effects of grain shape, size and arrangement are not taken into account.

Predictions from the polycrystal model of Asaro & Needleman (1985) concerning the evolution of texture in simple shear of FCC polycrystals have been compared by Harren *et al.* (1989) against the existing experimental work of Williams (1962) on previously rolled copper. These authors have found that the first-order features of Williams's (1962) experimentally determined textures were captured by Asaro & Needleman's (1985) Taylor-type polycrystal model. In a recent paper, Harren & Asaro (1989) also attempt to evaluate the performance of the Taylor-type model of Asaro, Needleman and co-workers, but this time by comparison against finite element simulations of polycrystalline aggregates. However, in their Taylor type calculations as well as their finite element calculations they do not use the actual three-dimensional slip systems, but *idealized two-dimensional slip systems*.

Some limitations of these previous evaluations of the Taylor-type model of Asaro & Needleman follow. (*a*) There is no comparison of predicted stress–strain curves against actual experimental data, since no comprehensive data on both the stress–strain response and the evolution of texture for various modes of deformation on the same material are currently available in the literature. (*b*) The data of Williams (1962) on the evolution of texture in simple shear of copper are on a *pre-textured* material. Although Harren *et al.* (1989) did consider the effect of this pre-texture in their Taylor-type calculations, an evaluation of the accuracy of a polycrystalline model using experimental texture data from pre-textured material is substantially more complicated and prone to error, than an evaluation which uses data from annealed, initially 'isotropic' material. This is because of the inherent difficulties associated with an accurate characterization of the initial state (slip system orientations and deformation resistances) of deformed polycrystalline materials. (*c*) The finite element simulations use a simplified two-dimensional slip system structure, in place of the actual three-dimensional slip system structure.

The purpose of this paper is to report on our evaluation of (a slightly modified form of) the Taylor-type model of Asaro & Needleman (1985). Specifically we compare the predictions for the evolution of crystallographic texture and stress–strain curves in (1) simple compression and simple tension, (2) plane strain compression, and (3) simple shear of initially isotropic LFHC copper against (*a*) corresponding experiments, and (*b*) finite element calculations using the actual slip system structure for a FCC material with 12 $\{111\}\langle 110\rangle$ type slip systems. We believe ours to be the most extensive set of currently available experimental data which documents both the stress–strain response and the evolution of crystallographic texture for copper.

The plan of the paper is as follows. We introduce our notation in §2. The constitutive model is summarized in §3. In §4 we consider specific constitutive functions, propose a slip system hardening law for FCC crystals, and evaluate the hardening parameters for OFHC copper using the stress–strain data from a simple compression experiment. In §5 we give brief descriptions of our experiments, and compare the experimental results against corresponding simulations using the Taylor-type model. In this section we also describe our finite element simulations and compare the results against those obtained from the experiments and the Taylor model simulations. We close in §6 with some final remarks.

2. Notation

For the most part we shall use notation which is standard in modern continuum mechanics (Gurtin 1981):

$\boldsymbol{p}$	material point of a body in a reference configuration at time 0
$\boldsymbol{x} = \bar{\boldsymbol{x}}(\boldsymbol{p}, t)$	motion
$\boldsymbol{p} = \bar{\boldsymbol{p}}(\boldsymbol{x}, t)$	reference map
$\boldsymbol{F}(\boldsymbol{p}, t) \equiv \frac{\partial}{\partial \boldsymbol{p}} \bar{\boldsymbol{x}}(\boldsymbol{p}, t) \quad \det \boldsymbol{F}(\boldsymbol{p}, t) > 0$	deformation gradient
$\dot{\bar{\boldsymbol{x}}}(\boldsymbol{p}, t) \equiv \frac{\partial}{\partial t} \bar{\boldsymbol{x}}(\boldsymbol{p}, t)$	velocity
$\boldsymbol{v}(\boldsymbol{x}, t) \equiv \dot{\bar{\boldsymbol{x}}}(\bar{\boldsymbol{p}}(\boldsymbol{x}, t), t)$	spatial description of velocity
$\boldsymbol{L}(\boldsymbol{x}, t) \equiv \frac{\partial}{\partial \boldsymbol{x}} \boldsymbol{v}(\boldsymbol{x}, t)$	velocity gradient
$\boldsymbol{T}(\boldsymbol{x}, t)$	Cauchy stress
$\mathscr{I}$	fourth-order identity tensor
$\mathbf{1}$	second-order identity tensor.

For brevity, we omit the arguments $(\boldsymbol{x}, t)$, $(\boldsymbol{p}, t)$, etc., for the various field quantities listed above. Also, the inner product of two vectors $\boldsymbol{u}$ and $\boldsymbol{v}$ is denoted by $\boldsymbol{u} \cdot \boldsymbol{v}$. The tensor product of two vectors $\boldsymbol{u}$ and $\boldsymbol{v}$ is denoted by $\boldsymbol{u} \otimes \boldsymbol{v}$; it is the tensor which assigns to each vector $\boldsymbol{w}$ the vector $(\boldsymbol{v} \cdot \boldsymbol{w})\, \boldsymbol{u}$. The inner product of two (second rank) tensors $\boldsymbol{S}$ and $\boldsymbol{T}$ is defined by $\boldsymbol{S} \cdot \boldsymbol{T} = \operatorname{trace}(\boldsymbol{S}^{\mathrm{T}} \boldsymbol{T})$.

3. Constitutive model

The geneaology of the constitutive model for polycrystalline plasticity considered here may be traced to papers by Rice (1971), Hill & Rice (1972), Asaro & Rice (1977), Asaro (1983*a*, *b*), and Asaro & Needleman (1985).

We take the stress response at each macroscopic continuum polycrystalline material point to be the volume averaged response of the multitude of microscopic single crystalline grains comprising the material point. The essential assumptions in Asaro & Needleman's (1985) Taylor-type polycrystal model are that all grains have equal volume, and that the local deformation gradient in each grain is homogeneous and identical to the macroscopic deformation gradient $\boldsymbol{F}$ at the continuum material point level. Then, with $\boldsymbol{T}^{(k)}$ denoting the Cauchy stress in the kth crystal, these assumptions lead to:

$$\bar{\boldsymbol{T}} = \frac{1}{N} \sum_{k=1}^{N} \boldsymbol{T}^{(k)}, \tag{3.1}$$

where $\bar{\boldsymbol{T}}$ is the volume averaged stress, and N is the total number of grains comprising the material point.

The constitutive equation for the stress in each grain is taken as

$$\boldsymbol{T}^* = \mathscr{L}[\boldsymbol{E}^*], \tag{3.2}$$

where

$$\boldsymbol{E}^* \equiv \tfrac{1}{2}\{\boldsymbol{F}^{*\mathrm{T}}\boldsymbol{F}^* - \mathbf{1}\} \tag{3.3}$$

is an elastic strain measure, $\mathscr{L}$ is a fourth-order elasticity tensor, and

$$\boldsymbol{T}^* \equiv \boldsymbol{F}^{*-1}\{(\det \boldsymbol{F}^*)\,\boldsymbol{T}\}\,\boldsymbol{F}^{*-\mathrm{T}} \tag{3.4}$$

is the stress measure which is elastic work conjugate to the strain measure $\boldsymbol{E}^*$ defined above. Also, $\boldsymbol{T}$ is the symmetric Cauchy stress tensor in the grain, and $\boldsymbol{F}^*$ is a local elastic deformation gradient defined in terms of the local deformation gradient $\boldsymbol{F}$ (equal to the macroscopic deformation gradient by virtue of the Taylor assumption) and a local plastic deformation gradient $\boldsymbol{F}^{\mathrm{p}}$, with $\det \boldsymbol{F}^{\mathrm{p}} = 1$ (plastic incompressibility), by

$$\boldsymbol{F}^* \equiv \boldsymbol{F}\boldsymbol{F}^{\mathrm{p}-1}, \quad \det \boldsymbol{F}^* > 0. \tag{3.5}$$

The plastic deformation gradient is in turn given by the flow rule

$$\dot{\boldsymbol{F}}^{\mathrm{p}} = \boldsymbol{L}^{\mathrm{p}}\boldsymbol{F}^{\mathrm{p}}, \tag{3.6}$$

with

$$\boldsymbol{L}^{\mathrm{p}} = \sum_{\alpha} \dot{\gamma}^{\alpha}\boldsymbol{S}_{0}^{\alpha}, \quad \boldsymbol{S}_{0}^{\alpha} \equiv \boldsymbol{m}_{0}^{\alpha} \otimes \boldsymbol{n}_{0}^{\alpha}, \tag{3.7}$$

where $\boldsymbol{m}_0^{\alpha}$ and $\boldsymbol{n}_0^{\alpha}$ are *time-independent* orthonormal unit vectors which define, respectively, the slip direction and slip plane normal of the slip system α in a fixed reference configuration, and $\dot{\gamma}^{\alpha}$ is the plastic shearing rate on this slip system.

The local configuration for a grain defined by $\boldsymbol{F}^{\mathrm{p}}$ is an isoclinic relaxed configuration, and a plastic stress power per unit volume in this configuration may be defined by (Anand 1985)

$$\dot{w}^{\mathrm{p}} \equiv (\boldsymbol{C}^*\boldsymbol{T}^*)\cdot\boldsymbol{L}^{\mathrm{p}}, \quad \text{with} \quad \boldsymbol{C}^* \equiv \boldsymbol{F}^{*\mathrm{T}}\boldsymbol{F}^*. \tag{3.8}$$

Using (3.7*a*) and (3.8), we define a *resolved shear stress* τ^{α} for the slip system α through the relation

$$\dot{w}^{\mathrm{p}} = \sum_{\alpha} \tau^{\alpha}\dot{\gamma}^{\alpha}, \tag{3.9}$$

which yields

$$\tau^{\alpha} \equiv (\boldsymbol{C}^*\boldsymbol{T}^*)\cdot\boldsymbol{S}_0^{\alpha}. \tag{3.10}$$

For metallic materials the elastic stretches are usually infinitesimal, and under these conditions the resolved shear stress may be approximated by

$$\tau^{\alpha} \approx \boldsymbol{T}^*\cdot\boldsymbol{S}_0^{\alpha}. \tag{3.11}$$

With the resolved shear stress so defined, the plastic shearing rate on the slip system α is taken to be governed by a constitutive function

$$\dot{\gamma}^{\alpha} = \hat{\dot{\gamma}}^{\alpha}(\tau^{\alpha}, s^{\alpha}), \tag{3.12}$$

where and s^{α} is the slip resistance for the slip system α.

Finally, the slip resistance s^α is taken to evolve as

$$\dot{s}^\alpha = \sum_\beta h^{\alpha\beta}|\dot{\gamma}^\beta|, \tag{3.13}$$

where $h^{\alpha\beta}$ is the rate of strain hardening on slip system α due to a shearing on the slip system β.

We will come back to a discussion of specific forms for the shearing rate function $\hat{\dot{\gamma}}^\alpha$ and the hardening function $h^{\alpha\beta}$ in the next section.

We have developed a new fully implicit time-integration algorithm for the constitutive model discussed in this section. A brief discussion of the algorithm for Taylor-type calculations is presented in Appendix A. A detailed discussion of the algorithm and its implementation in a finite element program is given in a recent paper by Kalidindi *et al.* (1992). The computational procedures presented in that paper can be used in two types of finite element calculations: (*a*) where the integration point represents a material point in a polycrystalline sample and the constitutive response is given through a Taylor-type polycrystal model, and (*b*) where the integration point represents a material point in a single grain and the constitutive response is given through a single-crystal model without invoking the Taylor assumption. We use this latter capability in this paper to simulate 'nominally homogeneous' deformations of simple compression and tension, plane strain compression, and simple shear of a polycrystalline aggregate by using a multitude of single crystals. The results from such calculations which satisfy (in the 'weak' finite element sense) both compatibility and equilibrium in the aggregate, will be compared against results from Taylor-type calculations in which only compatibility between grains is satisfied, but equilibrium between grains is violated.

4. Specific constitutive functions

For large plastic deformations, it is usual practice to neglect the elastic response of polycrystalline aggregates. In the calculations presented in this paper, we retain the elastic response but neglect the elastic anisotropy of the FCC single crystals and take the elasticity tensor $\mathscr{L}$ to be given by

$$\mathscr{L} \equiv 2\mu\mathscr{I} + (\kappa - \tfrac{2}{3}\mu)\,\mathbf{1}\otimes\mathbf{1}, \tag{4.1}$$

where μ and κ are the elastic shear and bulk moduli respectively.

For the plastic shearing rate, equation (3.12), we use the widely used power-law form (Hutchinson 1976):

$$\dot{\gamma}^\alpha = \dot{\gamma}_0|\tau^\alpha/s^\alpha|^{1/m}\,\mathrm{sgn}\,(\tau^\alpha), \tag{4.2}$$

where $\dot{\gamma}_0$ is a reference shearing rate and m is a strain rate sensitivity parameter.

The specific form of the hardening matrix $h^{\alpha\beta}$ in equation (3.13) used here is

$$h^{\alpha\beta} = q^{\alpha\beta}h^{(\beta)} \quad \text{(no sum on } \beta), \tag{4.3}$$

where $h^{(\beta)}$ is a single slip hardening rate which we take to be given generically by

$$h^{(\beta)} = \hat{h}(s^\beta), \tag{4.4}$$

and $q^{\alpha\beta}$ is the matrix describing the latent hardening behaviour of a crystallite.

Following Asaro & Needleman (1985), for the 12 slip systems of FCC crystals, we take $q^{\alpha\beta}$ to be given by

$$q^{\alpha\beta} = \begin{pmatrix} A & qA & qA & qA \\ qA & A & qA & qA \\ qA & qA & A & qA \\ qA & qA & qA & A \end{pmatrix}, \tag{4.5}$$

where q is the ratio of the latent hardening rate to the self-hardening rate, and A is a 3×3 matrix fully populated by ones. In equation (4.5), systems $\{1, 2, 3\}$ are coplanar, as are systems $\{4, 5, 6\}$, $\{7, 8, 9\}$, and $\{10, 11, 12\}$. Thus the ratio of the latent hardening rate to the self-hardening rate for coplanar slip systems is unity.

Next, motivated by the work of Brown *et al.* (1989), we consider the following specific form of the constitutive function $\hat{h}(s^\beta)$ for the single slip hardening rate in equation (4.4):

$$h^{(\beta)} = h_0\{1 - s^\beta / s_s\}^a, \tag{4.6}$$

where h_0, a, and s_s are slip system hardening parameters which are taken to be identical for all slip systems. In this saturation form of the single slip hardening rate, we take the saturation value s_s to be a constant. This saturation value should in general be an increasing function of the strain rate. This would account for a rate sensitivity of the rate of strain hardening, but at low temperatures and moderate strain rates this is a second-order effect.

These hardening parameters for annealed OFHC copper were found by curve-fitting the predicted stress–strain curve from the Taylor model for the case of uniaxial compression to corresponding experimental data. The copper was heat-treated at 800 °C for 1 h in an inert atmosphere. This heat treatment yields a reasonably random distribution of grain orientations for most commercial OFHC copper stock. In the numerical simulations, we took the latent hardening parameter in equation (4.5) to have a value $q = 1.4$, and the reference strain rate in equation (4.2) to have a value $\dot{\gamma}_0 = 0.001\ \mathrm{s}^{-1}$. The slip system rate sensitivity m in equation (4.2) is taken to be equal to the macroscopic strain rate sensitivity of 0.012, which was determined from a strain rate jump experiment in compression at room temperature.

Experimental measurements of texture of the annealed (and deformed) copper were obtained by X-ray irradiation using a Rigaku RU200 diffractometer. Specimens for texture measurement were prepared by hand grinding and then electro-polishing in an agitated solution of 250 ml H_3PO_4, 250 ml ethanol, 50 ml propanol, 500 ml distilled water, and 3 g urea for 3–5 min at power level of 1.5 A and 5–7 V. The resulting surfaces were free of visible grind marks. Partial pole figures were generated by using the Schulz reflection method on the {111}, {200}, (220}, and {311} crystallographic planes using copper K_α radiation. The irradiated surfaces were approximately 5.0 mm × 1.2 mm in area, and since the average grain diameter of the OFHC copper was approximately 60 µm, a typical irradiated surface would sample more than 1600 grains.

The pole figure data in their raw form are uncorrected and are in the form of discretized intensities as a function of goiniometer position angles. To process the raw data, the Preferred Orientation Package of Los Alamos (Kallend *et al.* 1989) was used. Each measured pole figure was corrected for background and defocusing. In addition, spherical harmonics were used to extrapolate the outer 15° of each pole figure. All pole figures presented in this paper are equal-area projections of the specified crystallographic planes.

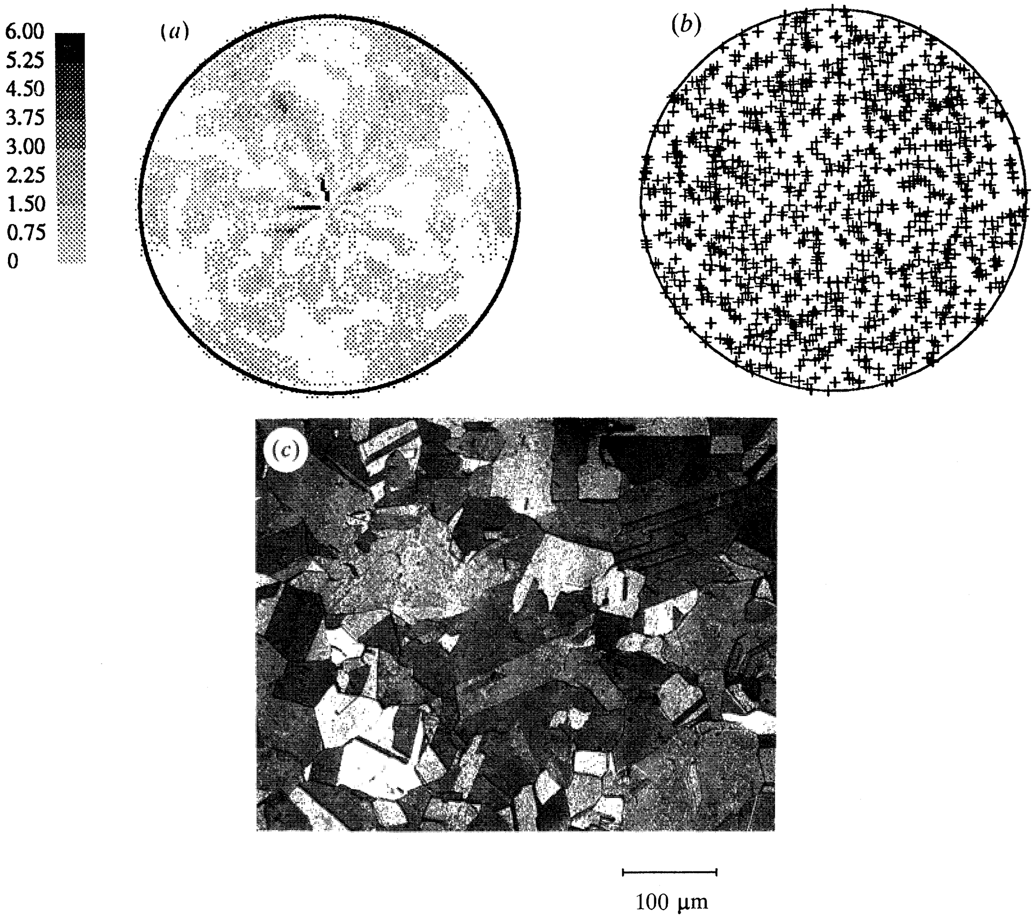

Figure 1. (*a*) Initial experimental {111} (equal area projection) pole figure of annealed OFHC copper. (*b*) Representation of initial 'isotropic' texture by 300 crystals. (*c*) Photomicrograph of annealed copper.

The annealed OFHC copper is assumed to have an isotropic initial texture, and this texture in our calculations is represented by a set of 300 crystals whose orientations are extracted from Kallend *et al.* (1989). Figure 1 shows a comparison of the {111} (equal-area projection) pole figures corresponding to the assumed initial set of crystal orientations, and an actual texture measurement from an annealed specimen. This figure also shows a photomicrograph of a polished and etched annealed specimen; the copper grains are reasonably equiaxed.

The values of the elastic shear and bulk moduli for copper that we have used in our calculations are $\mu = 46.5\ \mathrm{GPa}$ and $\kappa = 124\ \mathrm{GPa}$. The values of the material parameters in the single slip hardening equation (4.6) for annealed OFHC copper estimated by our curve-fitting procedure are

$$h_0 = 180\ \mathrm{MPa}, \quad s_s = 148\ \mathrm{MPa}, \quad a = 2.25, \tag{4.7}$$

together with an initial value of the slip resistance of

$$s_0 = 16\ \mathrm{MPa}, \tag{4.8}$$

which serves as an initial condition for equations (3.13).

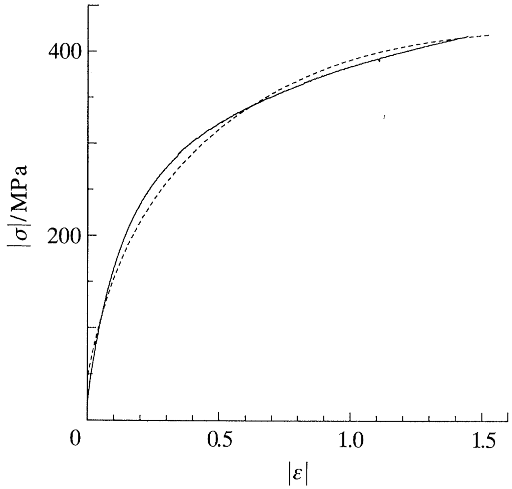

Figure 2. Axial stress against logarithmic axial strain response in simple compression. ——, Experiment; ––––, simulation.

The correspondence between the stress–strain results from a Taylor-type simulation of a simple compression experiment with the experimental data (from which the material parameters were determined) is shown in figure 2. The agreement is reasonable.

5. Evaluation of constitutive model

In this section we evaluate the Taylor-type constitutive model for polycrystalline materials under consideration by comparing the predictions for stress–strain curves and the evolution of crystallographic texture in (1) simple compression and simple tension, (2) plane strain compression, and (3) simple shear of initially isotropic OFHC copper against corresponding (*a*) experiments, and (*b*) finite element calculations.

(*a*) *Comparison against experiments*

All our experiments have been performed at room temperature and quasi-static rates of deformation. (The experimental data are available from the authors upon request.) The compression, tension, and plane strain compression experiments were conducted at a true strain rate of 0.001 s^{-1}, while the simple shear experiments were conducted at a shear strain rate of 0.0017 s^{-1}. Complete details of the experimental procedures are given in Bronkhorst (1991).

(i) *Simple compression and tension*

The initial height to diameter ratio of the cylindrical compression specimens was 1.5. Teflon film was used for lubrication of the ends of the specimen during compression. Four experiments were performed to final true plastic strain levels of -0.20, -0.48, -0.99, and -1.53. The stress–strain data for the specimen deformed to a true plastic strain of -1.53 as well as the fitted response (as discussed in §4, and below) is given in figure 2.

In our simulations we have approximated the compression experiments with the

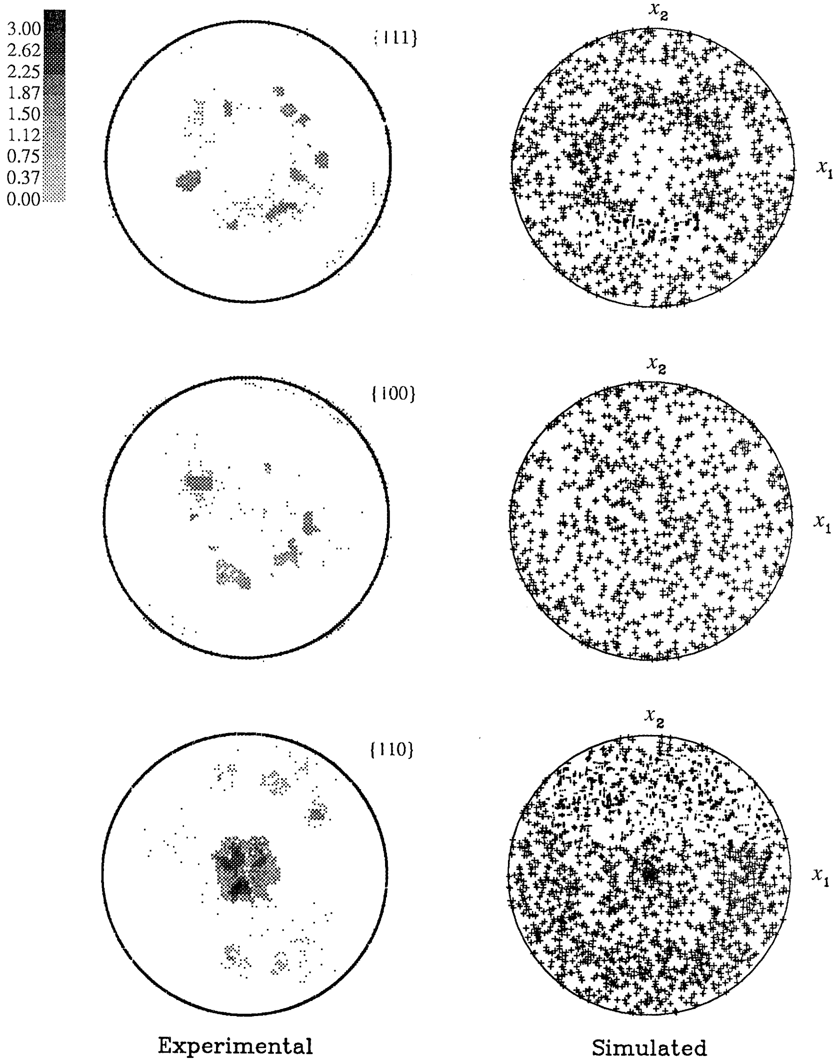

Figure 3(*a*). Experimental and simulated crystallographic texture for simple compression to $\epsilon_{33} = -0.20$.

following isochoric motion with respect to a rectangular cartesian coordinate system with origin $\boldsymbol{o}$ and orthonormal base vectors $\{\boldsymbol{e}_i \,|\, i = 1, 2, 3\}$:

$$\boldsymbol{x} = \exp\{-\tfrac{1}{2}\dot{\epsilon}t\}\, p_1\, \boldsymbol{e}_1 + \exp\{-\tfrac{1}{2}\dot{\epsilon}t\}\, p_2\, \boldsymbol{e}_2 + \exp\{\dot{\epsilon}t\}\, p_3\, \boldsymbol{e}_3, \tag{5.1}$$

with $\dot{\epsilon} = -0.001\ \mathrm{s}^{-1}$. The response from the Taylor model to this isochoric motion is the volume averaged stress deviator $\bar{\boldsymbol{T}}' = \bar{\boldsymbol{T}} + p\boldsymbol{1}$, with p an undetermined pressure. Since the lateral tractions in the experiments are zero, the axial Cauchy stress may be approximated by

$$\sigma \equiv \bar{T}_{33} = \bar{T}'_{33} - p, \quad \text{with} \quad p = \tfrac{1}{2}(\bar{T}'_{11} + \bar{T}'_{22}), \tag{5.2}$$

and it is the absolute value of the stress component σ which is plotted in figure 2.

(A comparison of this approximate calculation for simulating simple compression

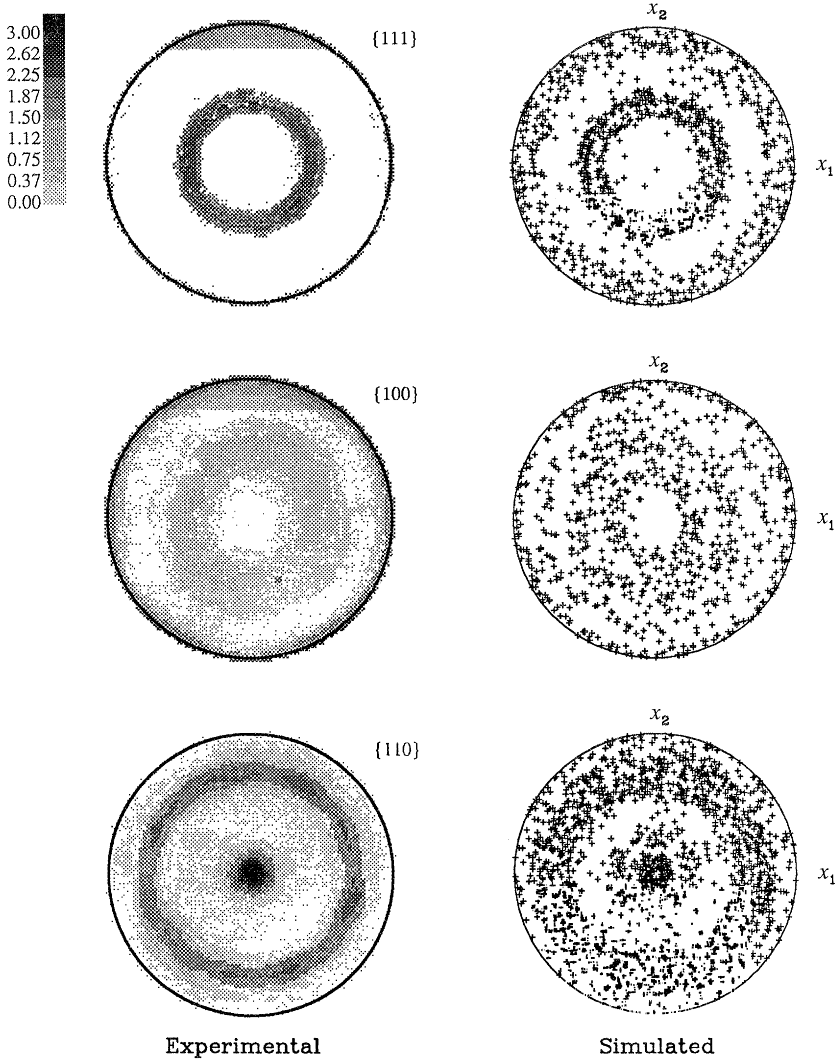

Figure 3 (*b*). Experimental and simulated crystallographic texture for simple compression to $\epsilon_{33} = -0.49$.

and tension against a single 3D finite element calculation that (*a*) uses a Taylor-type polycrystal model, (*b*) does not assume axisymmetry, and (*c*) satisfies traction free boundary conditions on the lateral surfaces, reveals that the discrepancy between the two calculations is very small.)

The experimental and simulated {111}, {100}, and {110} (equal-area projection) pole figures at each of the four levels of plastic strain are given in figure 3*a*–*d*. The agreement is reasonable. We note that simple compression produces a texture which is axi-symmetric with respect to the loading axis, and that the grains of the polycrystal rotate such that {110} planes become perpendicular to the loading axis. This is clear from the experimental {110} pole figures in figure 3 where there exists a strong pole along the direction of loading.

We also observe that there is a small hole in the centre of the simulated {110} pole

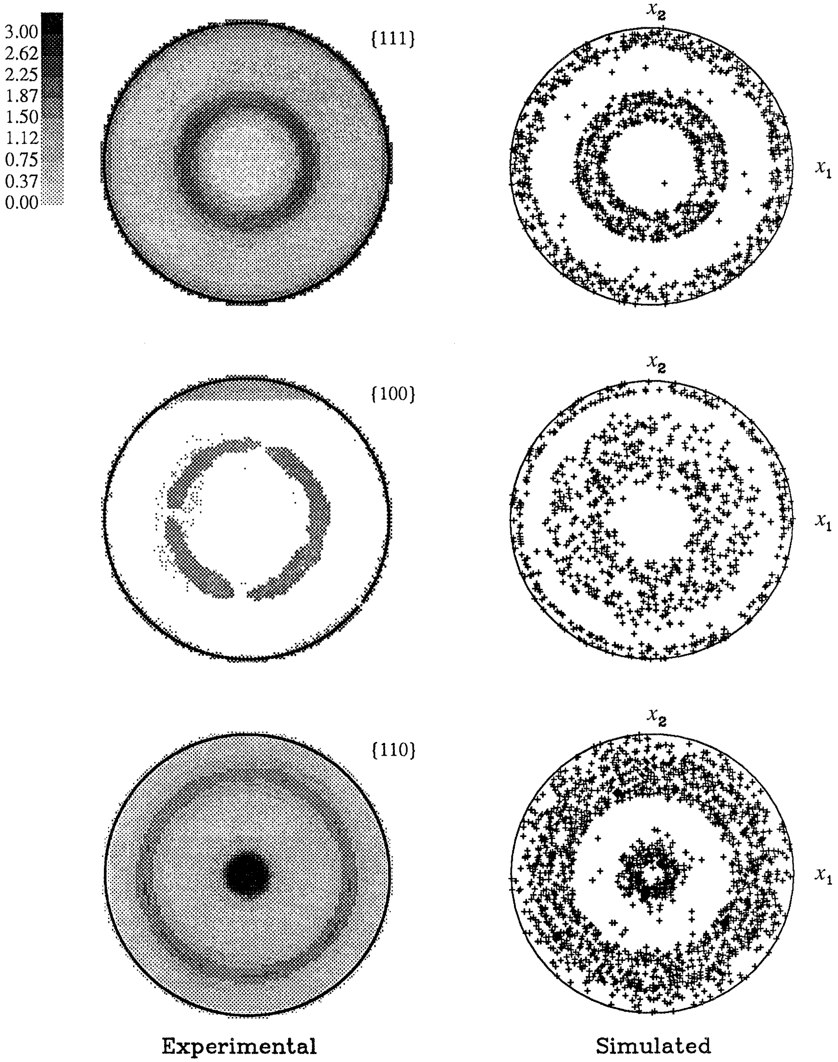

Figure 3 (*c*). Experimental and simulated crystallographic texture for simple compression to $\epsilon_{33} = -0.99$.

figures in figure 3*c* and *d*, whereas this feature is not present in the experimental results. This deficiency in the prediction from the Taylor model is believed to be a consequence of the strong kinematical constraint on the deformation of the individual grains of the polycrystal in this model. As we shall see later (figure 16), when simple compression is simulated by using finite element calculations which relax the constraints on the deformation in the individual grains by satisfying compatibility and equilibrium, no hole in the {110} pole figures is predicted.

A tension experiment was performed to a true plastic strain level of 0.37. We were limited to this relatively small strain in this experiment due to the onset of diffuse necking. The experiment was approximated with the isochoric motion (5.1), but with $\dot{\epsilon} = 0.001\ \mathrm{s}^{-1}$. The response $\sigma \equiv \bar{T}_{33}$ (equation (5.2)) from the Taylor model to this isochoric motion is compared with the experimental stress–strain curve in figure 4*a*.

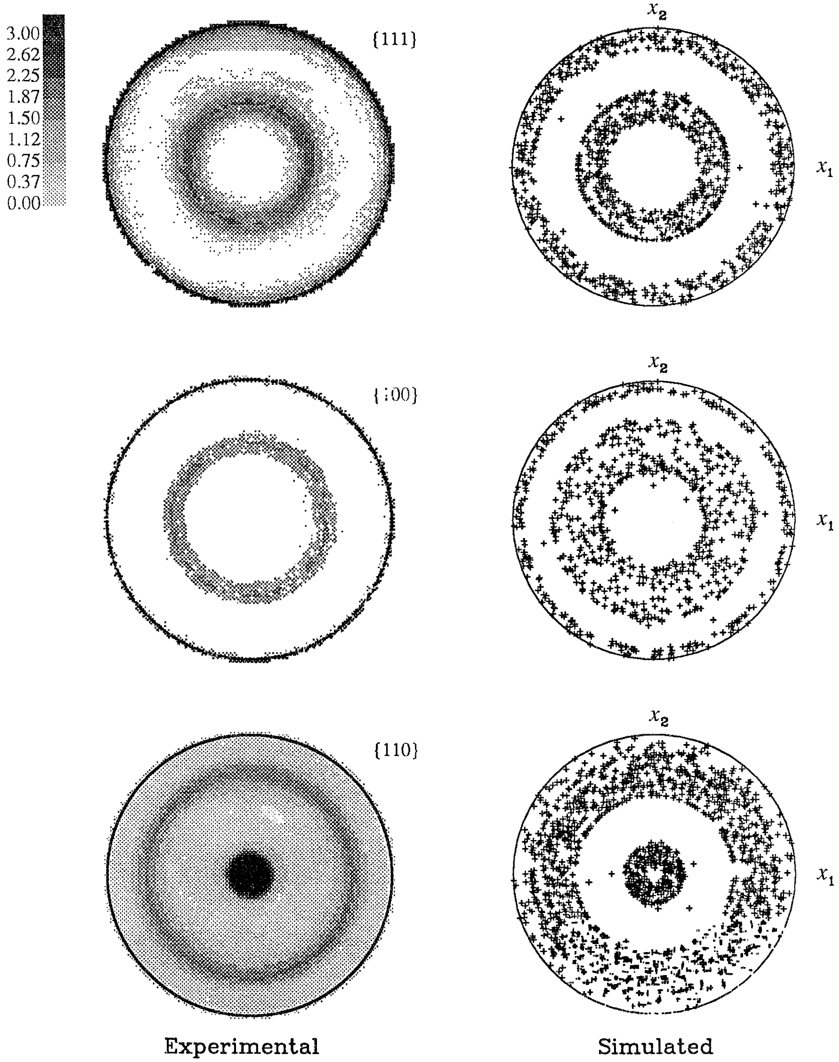

Figure 3 (*d*). Experimental and simulated crystallographic texture for simple compression to $\epsilon_{33} = -1.53$.

We see that the model under-predicts the stress–strain response to simple tension. This is to be expected in part, because in determining the hardening material parameters of the model we have used the compression data (which is for a much larger strain range, figure 2), and not the tension data. To illustrate this point, we show in figure 4*b* the simulation with s_s (equation (4.7)) equal to 187 MPa instead of 148 MPa and observe that we obtain a much better fit to the tension experiment to a strain of 0.5. However, we shall not use this higher value of s_s in our subsequent calculations, since most of our experiments are to much larger strains, and the material parameters estimated from the compression experiments are more representative.

We note that upon plotting the compression and the tension experimental stress–strain curves together in figure 5*a*, the tension flow curve lies above the

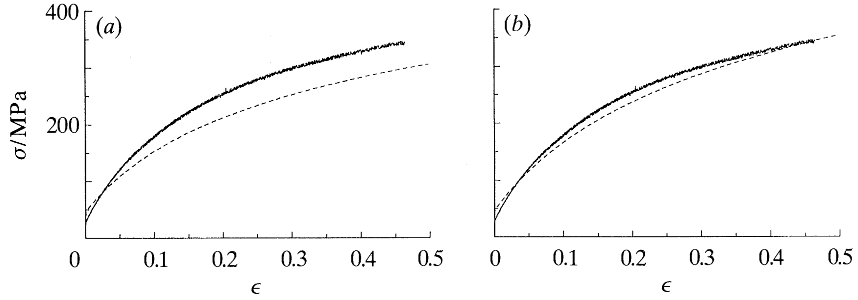

Figure 4. Axial stress against logarithmic axial strain response for simple tension. (*a*) Simulation using parameters evaluated from simple compression experiment to large strains. (*b*) Simulation using new parameters (s_s = 187 MPa instead of 148 MPa) that provide a better fit to a strain of 0.5. ——, Experiment; – – – –, simulation.

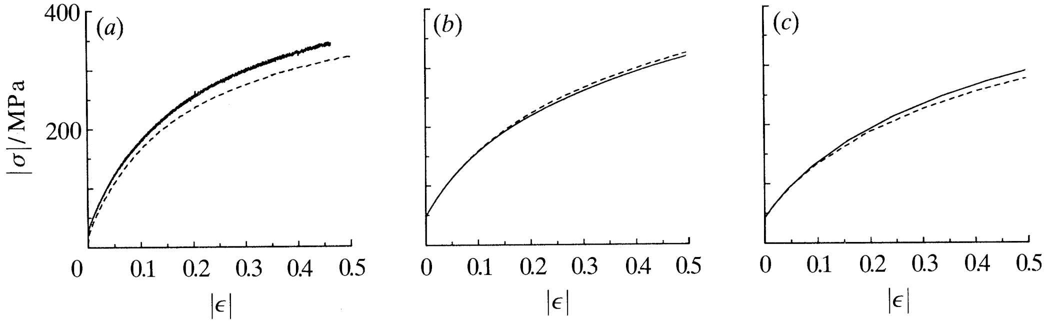

Figure 5. (*a*) Axial stress against logarithmic axial strain response for simple compression and simple tension. (*b*) Simulation using the Taylor model. (*c*) Simulation using finite element calculations. ——, Simple tension; – – – –, simple compression.

compression flow curve. However, the stress–strain response simulated by using the Taylor model, shown in figure 5*b*, is just the opposite – the simulated compression curve is slightly higher than the simulated tension curve. We believe that this discrepancy can also be attributed to the Taylor assumption because it ignores all grain interaction effects. As we shall see later, when simple tension and compression are simulated by using the finite element method, the flow stress relationship between tension and compression observed experimentally, is also obtained numerically.

The experimental and simulated pole figures at a plastic strain level of 0.37 are compared in figure 6 and we note that there is a good agreement between them. This figure shows that simple tension also produces a texture which is axi-symmetric with respect to the loading axis. In tension there are two dominant components of texture. From the {111} and {100} pole figures in figure 6 we note that there is a tendency of the grains of the polycrystal to rotate during deformation such that either {111} or {100} planes become perpendicular to the loading axis.

(ii) *Plane strain compression*

The dimensions of the plane strain compression specimens were 6.35 mm in the compression direction ($\boldsymbol{e}_3$), 9.53 mm in the free direction ($\boldsymbol{e}_2$), and 14.73 mm in the constrained direction ($\boldsymbol{e}_1$). The specimen was lubricated with both teflon film as well

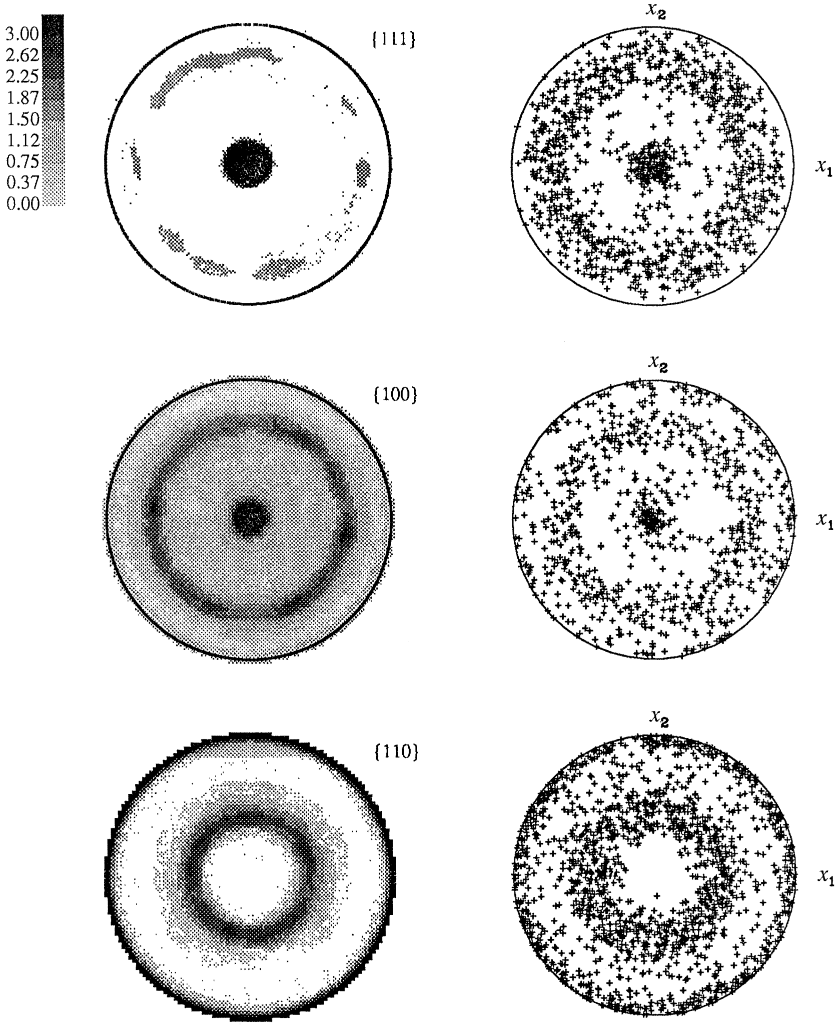

Experimental **Simulated**

Figure 6. Experimental and simulated crystallographic texture for simple tension to $\epsilon_{33} = 0.37$.

as a $\mathrm{MoS_2}$, and the sliding contact surfaces of the plane strain compression (channel die) fixture were also lubricated with the $\mathrm{MoS_2}$ lubricant. Four experiments were performed to final true plastic strain levels of -0.21, -0.52, -1.01, and -1.54.

For our simulations we have approximated the plane strain compression experiments with the following isochoric motion:

$$\boldsymbol{x} = p_1\boldsymbol{e}_1 + \exp\{-\dot{\epsilon}t\}\,p_2\boldsymbol{e}_2 + \exp\{\dot{\epsilon}t\}\,p_3\boldsymbol{e}_3, \tag{5.3}$$

with $\dot{\epsilon} = -0.001\ \mathrm{s}^{-1}$. The response from the Taylor model to this isochoric motion is the volume averaged stress deviator $\bar{\boldsymbol{T}}'$. Since the traction in the $\boldsymbol{e}_2$ direction in the experiments is zero, the axial average Cauchy stress is approximated by

$$\sigma \equiv \bar{T}_{33} = \bar{T}'_{33} - p, \quad \text{with} \quad p = \bar{T}'_{22}, \tag{5.4}$$

and it is the absolute value of this stress component σ which is plotted in figure 7,

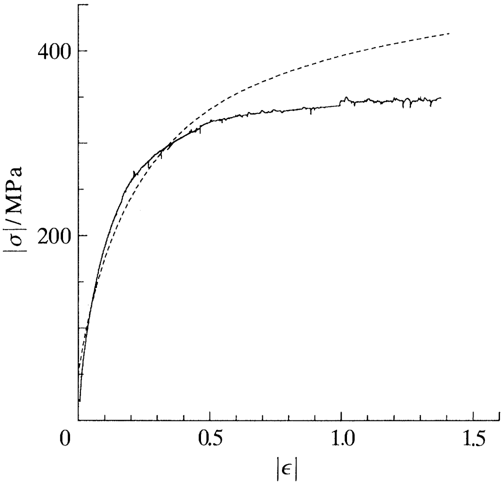

Figure 7. Stress against logarithmic strain response for plane strain compression. ——, Experimental; ----, simulation.

and compared with the experimental result. The experimental and simulated pole figures at each of the four levels of plastic strain are shown in figure 8*a*–*d*.

The agreement between the experimental and simulated textures is reasonable, however, as can be seen in figure 7, the model over-predicts the experimental flow curve for plane strain compression at large strains. For insight into this problem we have examined the microstructure of the deformed copper at different stages of deformation. Each of the deformed plane strain compression specimens was sectioned, polished, etched and examined metallographically. The resulting photomicrographs are shown in figure 9. In this figure, the constraint direction is out of the page and the compression direction is vertical. In figure 9*a*, at a true strain of -0.21, the grains are still reasonably equiaxed. Figure 9*b* shows the microstructure at a true strain of -0.52. At this stage the grains have been flattened, and localized bands of deformation can be observed within individual grains. The initiation of such micro-shear bands occurs somewhere between true strain levels of -0.21 and -0.52. This also approximately corresponds to the deformation level at which the simulated stress–strain response begins to diverge from the experimental measurement. The intensity of these micro-shear bands continues to increase as deformation progresses, and at some point between true strain levels of -1.00 (figure 9*c*) and -1.54 (figure 9*d*), macro-shear bands which cross grain boundaries have formed. In spite of such inhomogeneities in the deformation field the Taylor model performs reasonably well (figure 8) in predicting the evolution of crystallographic texture of copper during plane strain compression. This is attributable to the facts that up to the strain levels examined, the volume fraction of the material within the shear band regions is too small to give rise to a separate texture component, and that these localized regions do not significantly influence the orientation of the material outside these regions (Hirsch *et al.* 1988).

Comparing the predicted {111} pole figures with the corresponding measurements in figure 8*c* and *d*, we observe that while the measured texture exhibits a diffuse dumbbell like shape which becomes increasingly pronounced with increasing deformation, the texture predicted by the Taylor model exhibits a sharp elliptical

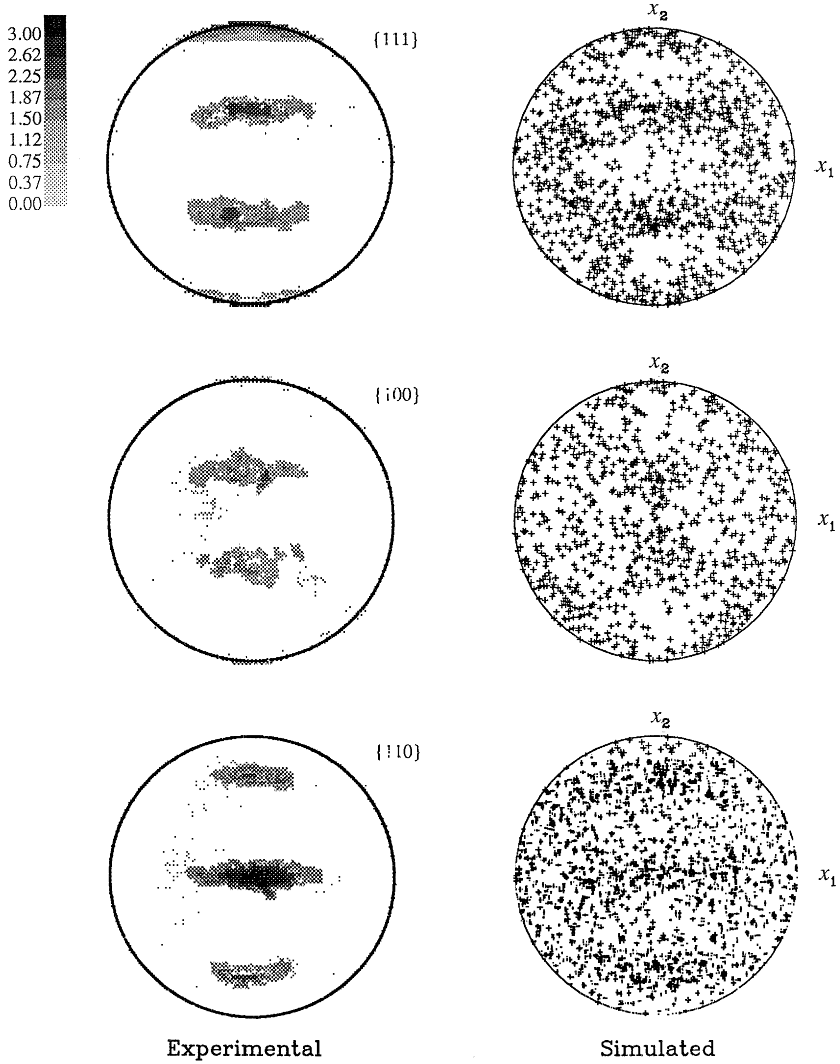

Figure 8(*a*). Experimental and simulated crystallographic texture for plane strain compression to $\epsilon_{33} = -0.21$.

shape. As we shall see later (figure 20), predictions from our finite element simulations for this experiment capture this dumbbell like shape in the {111} pole figures of the measured texture in plane strain compression.

(iii) *Simple shear*

A schematic of the double-planar-shear specimens used to approximate simple shear is shown in figure 10. The specimens were deformed by displacing the centre rail relative to the edge rails in a direction parallel to the channels. To generate shear stress versus shear strain data, a gauge section height (h) of 3.30 mm and a thickness (δ) of 2.03 mm were used. These gauge section dimensions minimize edge effects which are invariably present in a specimen of this type. Strain was measured locally, away from the edges, by printing a square grid pattern on the surface of the gauge

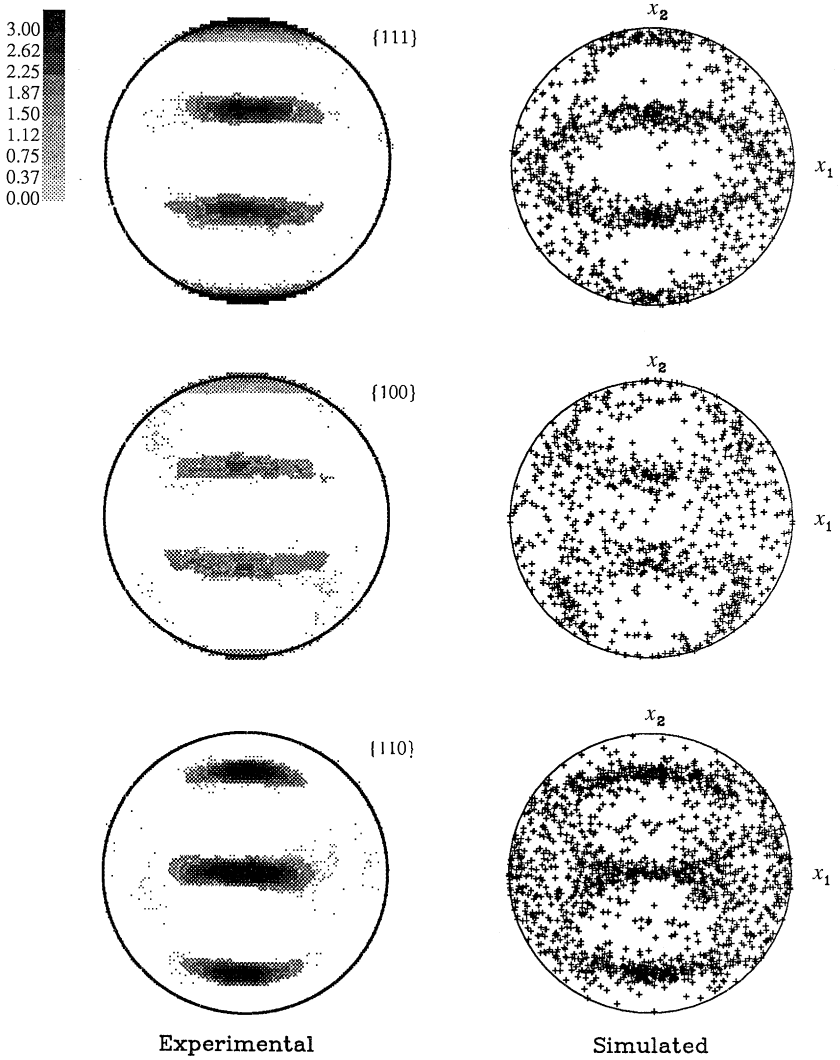

Figure 8(*b*). Experimental and simulated crystallographic texture for plane strain compression to $\epsilon_{33} = -0.52$.

sections and taking magnified photographs (25–40 ×) during deformation. The resulting shear stress against shear strain data are shown in figure 11. These experiments approximate the simple shearing motion

$$\boldsymbol{x} = \boldsymbol{p} + (\dot{\gamma}t)\, p_2\, \boldsymbol{e}_1, \tag{5.5}$$

with $\dot{\gamma} = -0.0017\ \mathrm{s}^{-1}$. The shear stress $|\bar{T}_{12}|$ and normal stresses $(\bar{T}_{22}, \bar{T}_{11})$ calculated using the Taylor model are also shown in figure 11. The agreement for the shear stress is reasonable. Note that in these experiments we were unable to measure the normal stresses.

For ease of experimental determination of the evolution of texture, we used specimens with large gauge sections: $h = 11.13$ mm, $\delta = 3.68$ mm. Five shearing experiments were performed to plastic shear strain levels of -0.26, -0.43, -0.75,

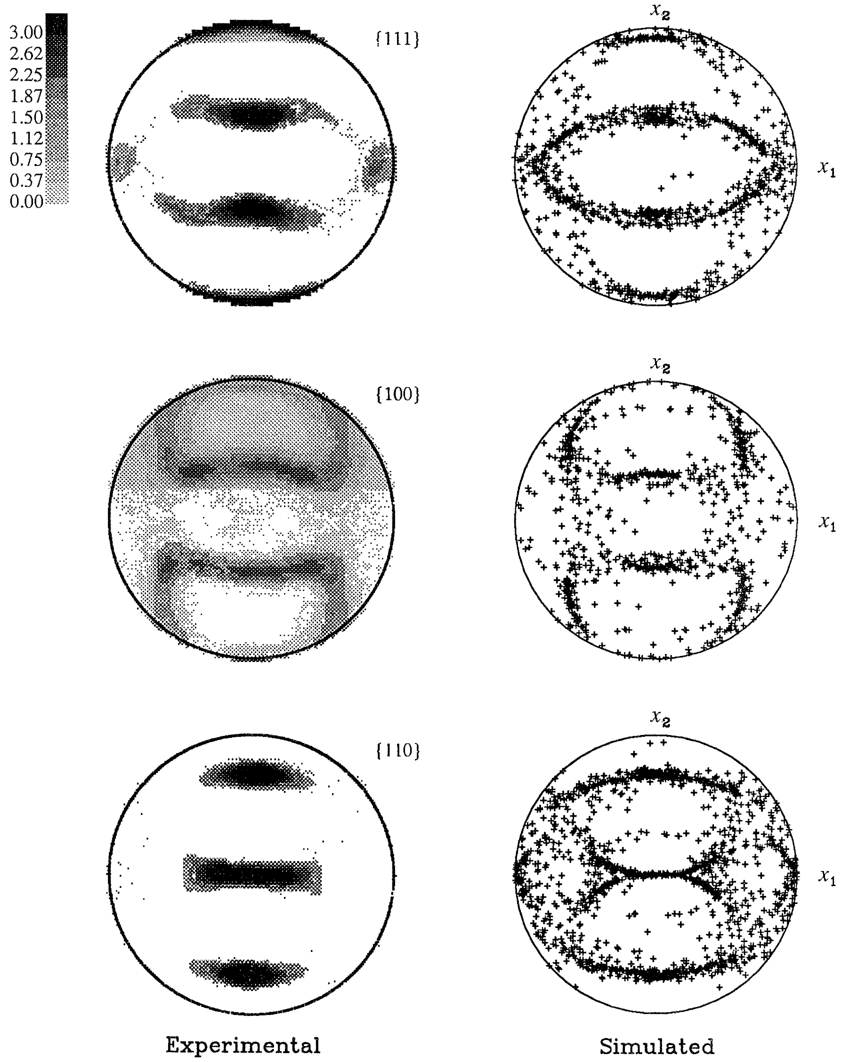

Figure 8 (*c*). Experimental and simulated crystallographic texture for plane strain compression to $\epsilon_{33} = -1.01$.

-1.16, -1.40, and the resulting texture was measured. The experimental and simulated pole figures for these experiments are shown in figure 12. There is good agreement between the simulated and the experimental textures, especially as the deformation progresses.

To measure the normal stress response, we have conducted a fixed-end thin-walled tubular torsion experiment to a plastic shear strain of -2.1. A schematic of the specimen geometry is shown in figure 13. A gauge section height of $h = 3.18$ mm was used to generate the stress–strain data. Strain was again measured photographically in a manner similar to the measurement technique for the planar simple shear experiments. The shear stress $|\bar{T}_{12}|$ and the normal stress $\bar{T}_{22}$ measured experimentally are also shown in figure 11. As is clear from this figure, although the shear stress

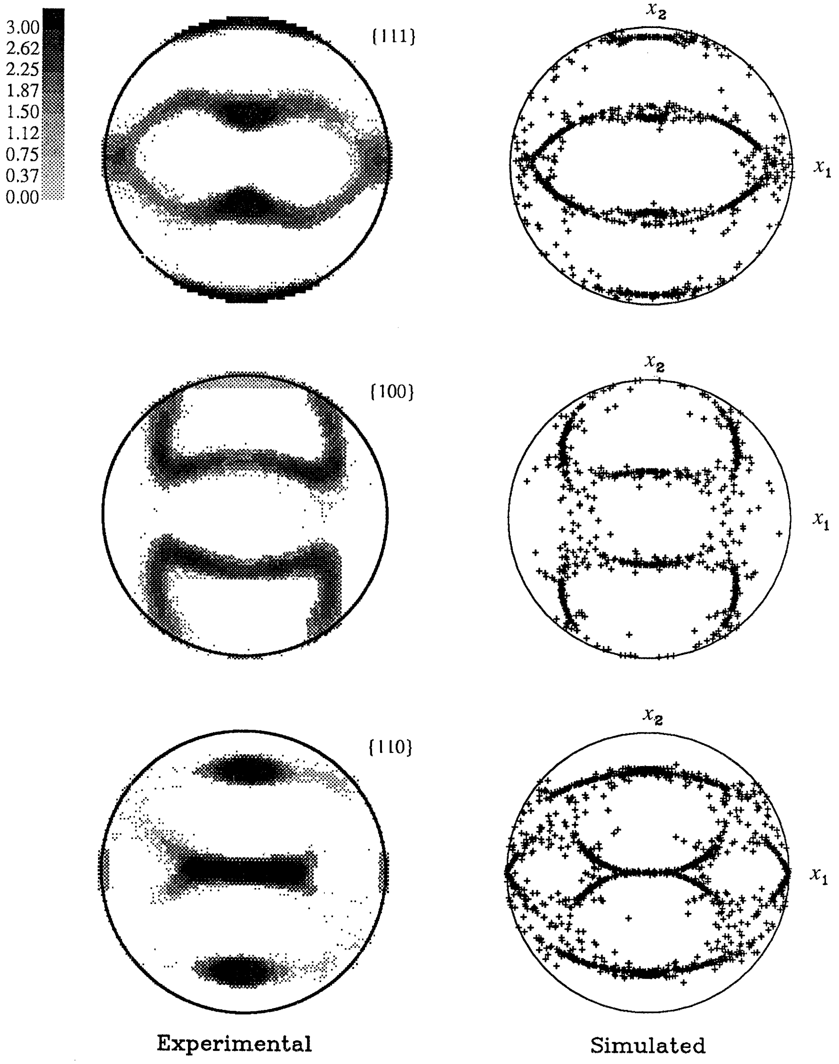

Figure 8(*d*). Experimental and simulated crystallographic texture for plane strain compression to $\epsilon_{33} = 1.54$.

against shear strain response is reasonably well predicted by the Taylor model, the normal stress is substantially overpredicted at strain levels above *ca*. 0.4.

For ease of experimental determination of torsion texture, we used a tubular torsion specimen with a gauge section height of $h = 12.7$ mm. The measured texture at a plastic shear strain of -1.50 is shown in figure 14 along with the predictions from Taylor-type simulations. In our simulation of the tubular torsion experiment, we have assumed the deformation to be simple shear as described in equation (5.5). The agreement between prediction and measurement is reasonable.

Upon comparing the experimental pole figures in figure 14 with those in figure 12*e* which show the measurements at a shear strain of -1.40 in a planar shear test, we note that although the measured textures from both the planar shear experiment and the tubular torsion experiment are in reasonable agreement with each other,

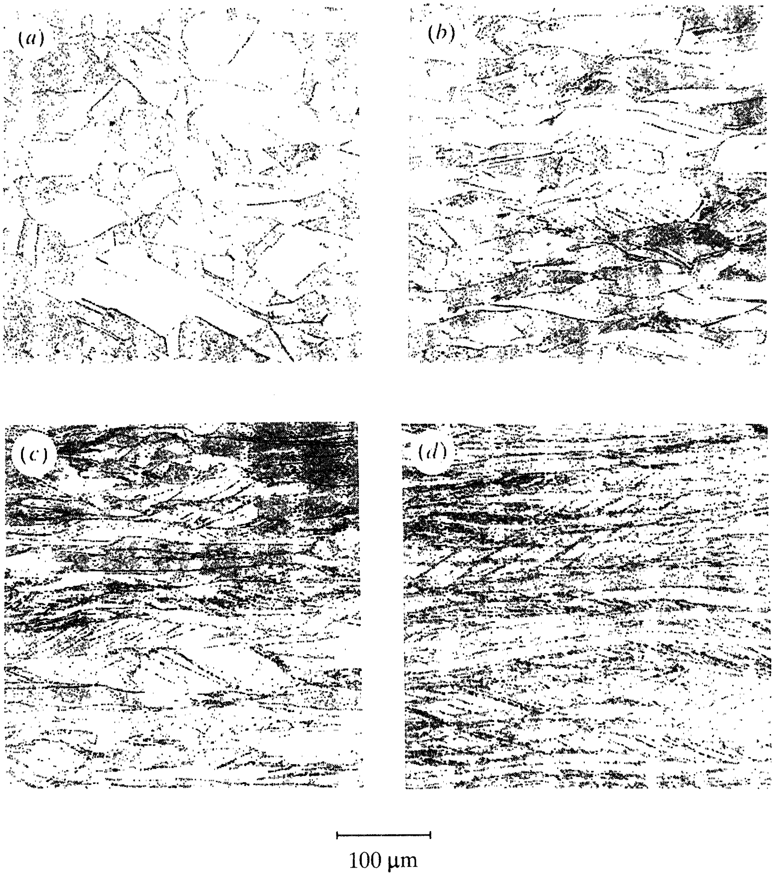

Figure 9. Photo-micrographs of OFHC copper deformed by plane strain compression: (a) $\epsilon_{33} = -0.21$; (b) $\epsilon_{33} = -0.52$; (c) $\epsilon_{33} = -0.1$; (d) $\epsilon_{33} = -1.54$.

there are some differences. We believe that these second-order differences can be attributed to the differences in the deformation modes of planar simple shear and torsion. The analytical and computational work of Harren *et al.* (1989) has shown that minor variations in the boundary conditions for shearing and torsion-type deformation modes can have some effect on the texture response of specimens, but may have a large effect on the stress–strain response.

(b) *Comparison against finite element calculations*

In the previous subsection we have compared the predictions from the Taylor-type model against experimental results. Recall that in this model the deformation gradient within each grain is assumed to have a uniform value throughout the aggregate. In this approximate model, compatibility is satisfied and equilibrium holds in each grain, but equilibrium is usually violated between grains. In this subsection we relax the uniform deformation gradient assumption, and carry out calculations for (1) simple compression and tension, (2) plane strain compression, and (3) simple shear for polycrystalline aggregates in which both compatibility and equilibrium are satisfied in the weak (finite element) sense, throughout the aggregate.

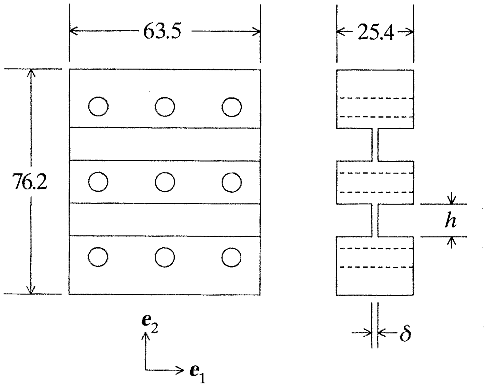

Figure 10. Planar simple shear specimen. Dimensions are in millimetres.

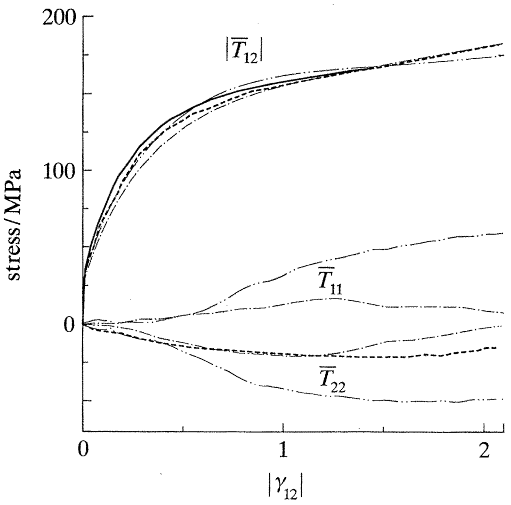

Figure 11. The response of stress components $|\bar{T}_{12}|$, $\bar{T}_{22}$, and $\bar{T}_{11}$ to amount of shear $|\gamma|$, in 'simple shear'. $\bar{T}_{11}$ was not measured experimentally. Experiment: – – –, tubular torsion; ——, planar simple shear. Simulation: –·–·–, FEM model; —··—··—, Taylor model.

In these calculations, because of the crystallinity of the material, the deformations are inherently inhomogeneous at the microlevel. To carry out such calculations, we (Kalidindi *et al.* 1992) have implemented our single crystal constitutive model and time-integration procedure in the finite element code ABAQUS (1990), and the simulations described below are carried out by using these computational procedures. In these numerical simulations, each element represents one crystal, and sets of initially 'random' grain orientations were assigned to the elements. As with the Taylor model simulations, the macroscopic stress–strain response and crystallographic texture are computed as volume averages over the entire aggregate. The crystallographic texture is arrived at by direct equal-area projection of the orientations of all the grains. To compare the results between the calculations using the Taylor model with those obtained using the finite element calculations, the Taylor simulations in this subsection are repeated with the same sets of Euler angles as are used in the finite element simulations.

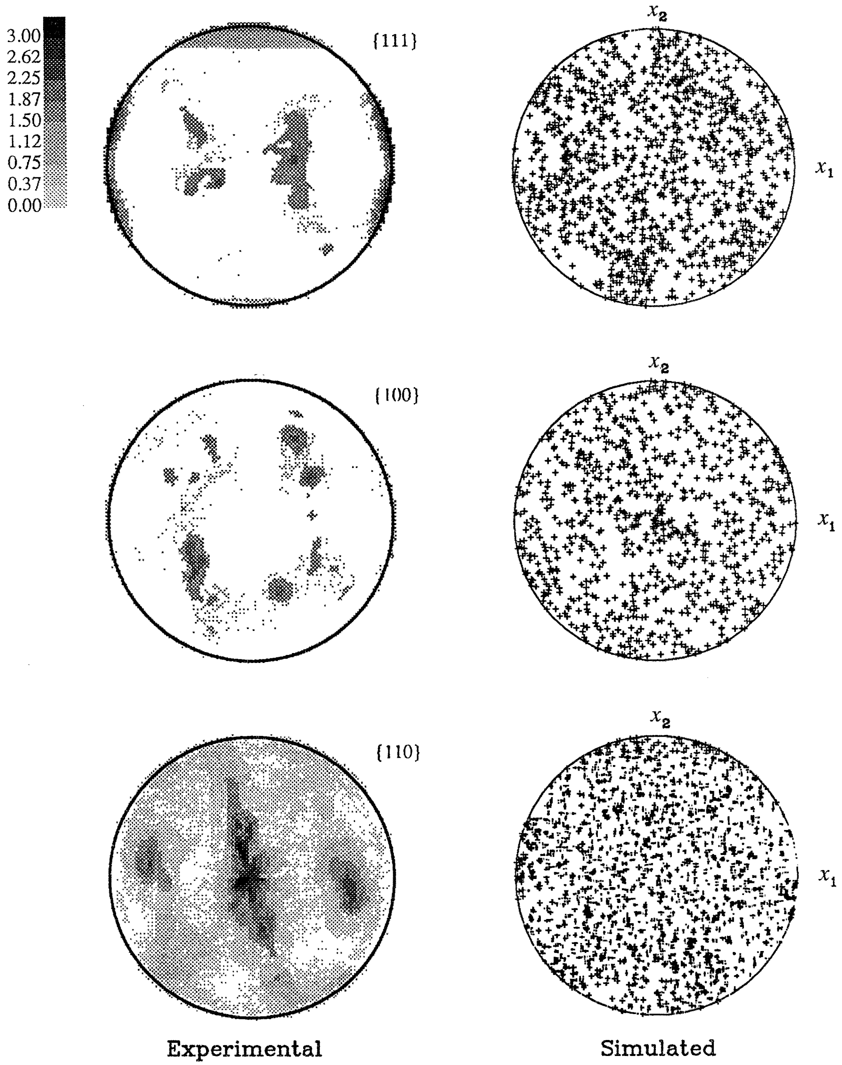

Figure 12(*a*). Experimental and simulated crystallographic texture for planar simple shear to $\gamma_{12} = -0.26$.

(i) *Simple compression and tension*

For the cases of simple compression and tension the initial mesh of 343 cubic ABAQUS-C3D8 (continuum, three-dimensional, eight-noded) elements used in the calculations is shown in figure 15*b*. As sketched in figure 15*a*, this mesh represents one-eighth of a rectangular parallelopiped specimen. Each element represents a single crystal, and a set of 343 initially 'random' grain orientations were assigned to these elements. The macroscopic (1, 2), (2, 3) and (3, 1)-planes of the meshed octant which are embedded in the full model are constrained to remain plane. The top (1, 2)-plane was constrained to remain plane, prescribed to be free from shear traction, and subjected to displacement boundary conditions which resulted in axial true strain rates of $\pm 0.001\ \text{s}^{-1}$. Deformed finite element meshes at late stages of the

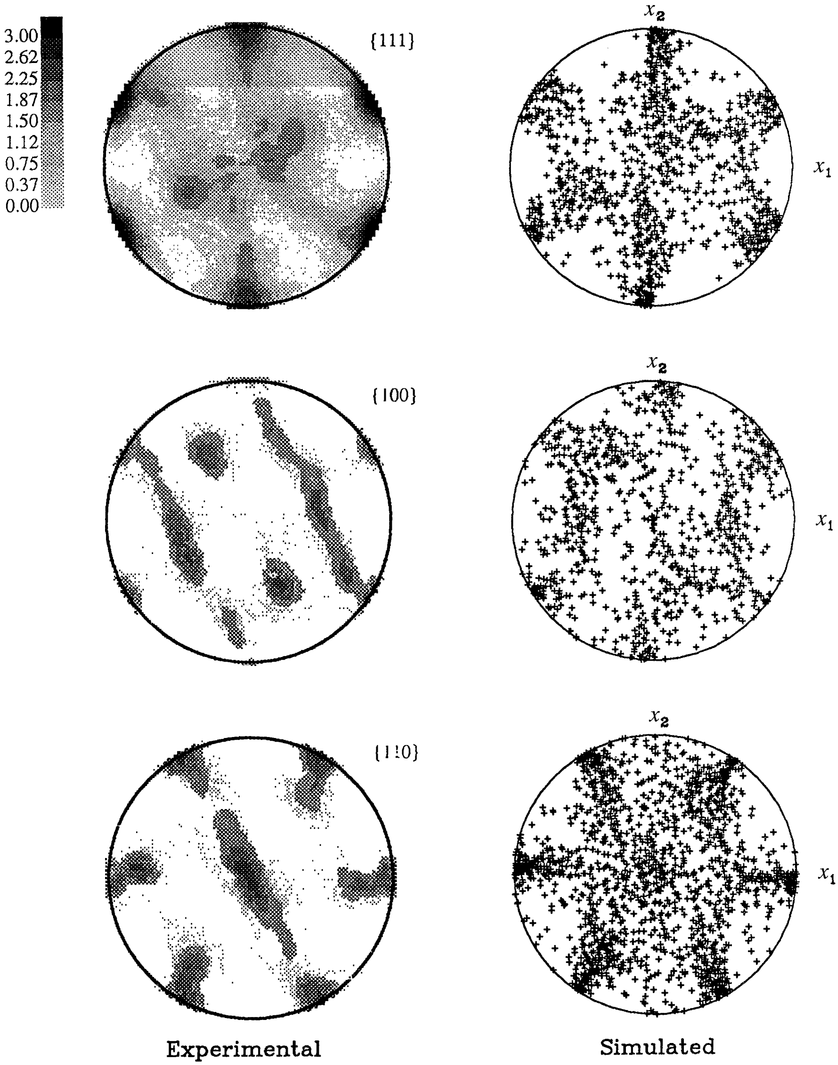

Figure 12(*b*). Experimental and simulated crystallographic texture for planar simple shear to $\gamma_{12} = -0.43$.

numerical experiments are shown in figure 15*c* for compression, and in figure 15*d* for tension. Since the outside surfaces of the finite element mesh are unconstrained, one obtains a remarkable 'orange peel' effect due to the differing orientations of the grains which intersect these free surfaces. The calculations had to be terminated when the grains became too distorted. This well-known 'orange peel' effect is also observed in our physical experiments.

Figure 5*c* shows the calculated stress-strain curves. Upon comparing these results with the actual experiments we note that in contrast to the results from the Taylor model, the finite element calculations correctly predict that the tension stress–strain curve is slightly higher than the compression stress–strain curve. Also, the stress–strain results from the finite element simulations (using the same values of slip hardening parameters as those used in Taylor-type model simulations) fall below

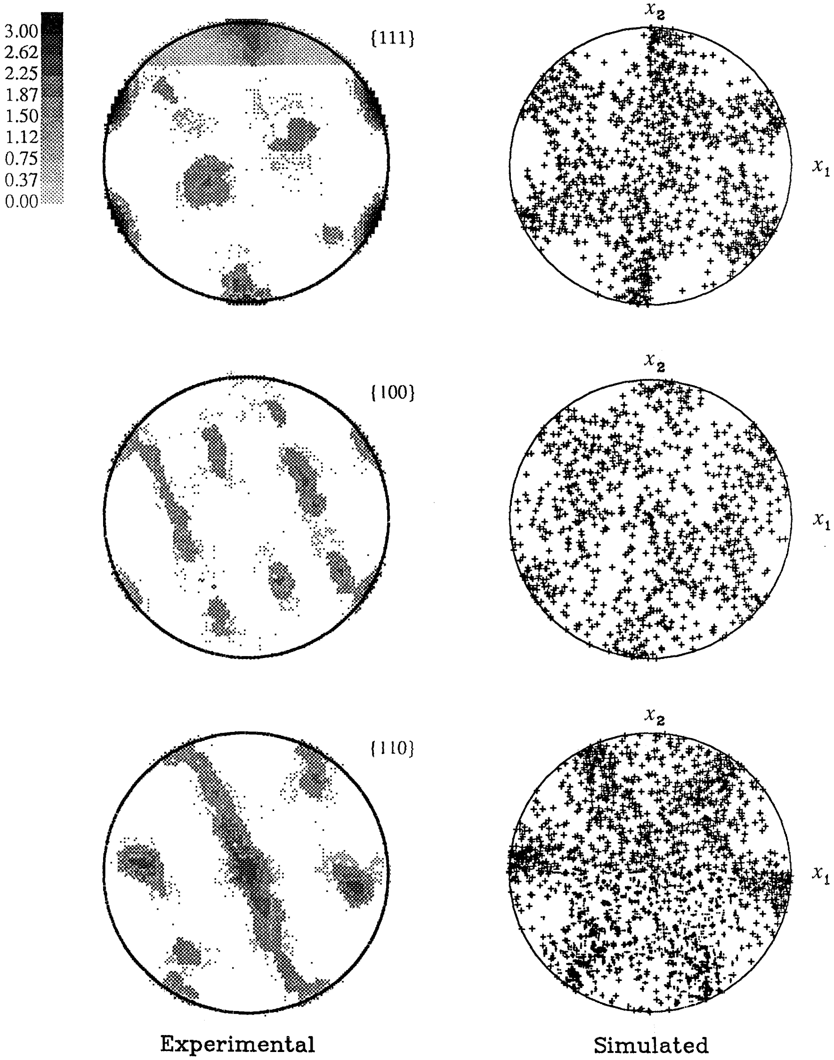

Figure 12(*c*). Experimental and simulated crystallographic texture for planar simple shear to $\gamma_{12} = -0.75$.

those from the Taylor-type model is absolute value, because of the richer displacement functions in the individual grains in the finite element model as compared with the uniform deformation gradient assumption in the Taylor method.

Figure 16 shows a comparison of the evolved {110} equal-area pole figures after an axial compressive strain of -1.10. As noted earlier, the Taylor model predicts that there are no {110} planes perpendicular to the loading axis – a ‘hole’ in the centre of the pole figure, whereas the experimental measurement does not exhibit such a hole. The {110} pole figure predicted by the finite element calculation also does not exhibit a hole in the centre. Further, the texture predicted by the Taylor model is sharper than that obtained from both the finite element model and the experimental result. This relative sharpness of the textures predicted by the Taylor-type model was also observed in {111} and {100} pole figures (not shown).

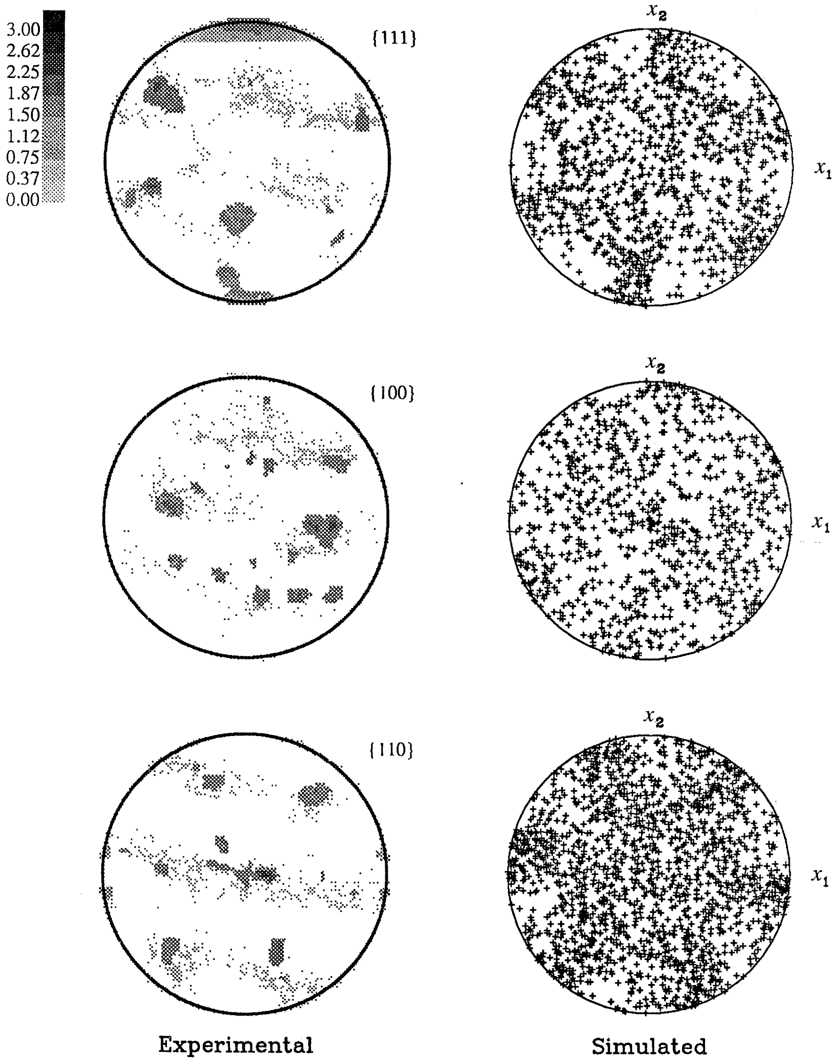

Figure 12 (*d*). Experimental and simulated crystallographic texture for planar simple shear to $\gamma_{12} = -1.16$.

Figure 17 shows a comparison of the evolved {111} pole figures after an axial tensile strain of 0.37. In this case, the predictions of Taylor-type model are in good agreement with the predictions from finite element simulations as well as the experimental measurements.

The results of our finite element calculations were not very sensitive to the manner in which the individual grains were assigned the initial Euler angles. Also, when we performed the calculations with only 100 elements and 100 initial grain orientations, instead of 343 elements and 343 grain orientations, we obtained very similar results for the stress–strain response and the evolution of texture, but the deformed mesh was heavily distorted.

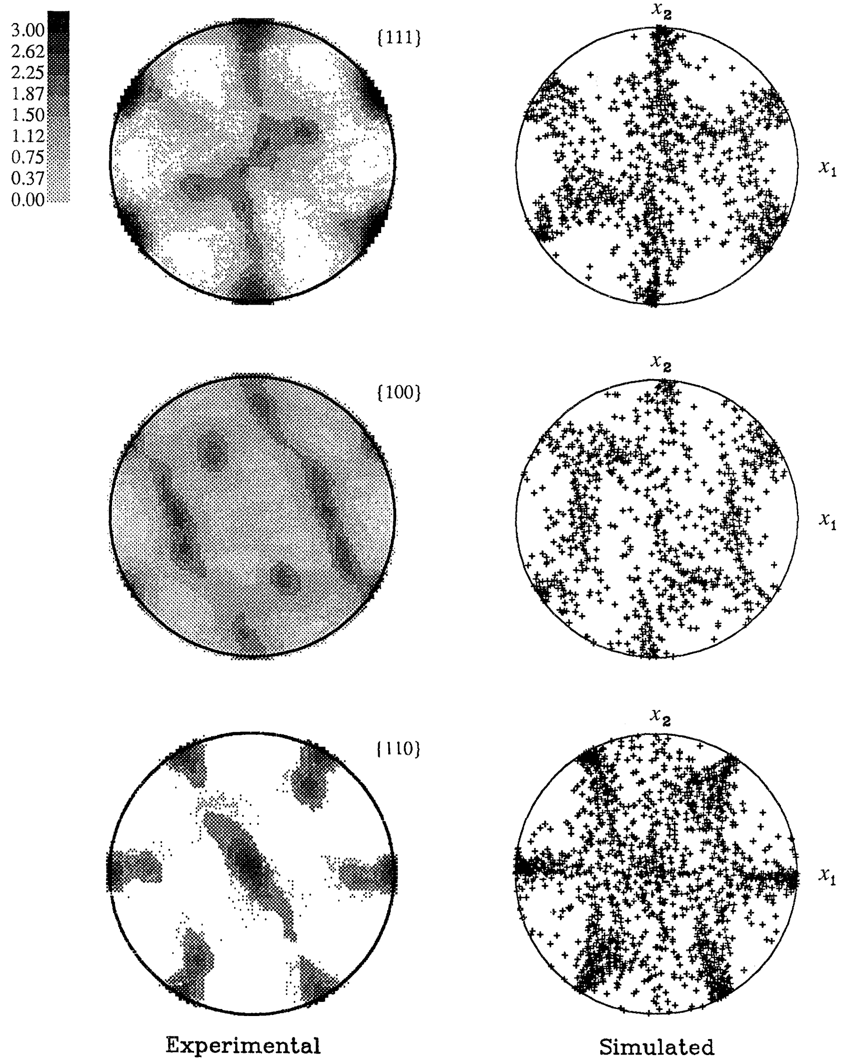

Figure 12 (*e*). Experimental and simulated crystallographic texture for planar simple shear to $\gamma_{12} = -1.40$.

(ii) *Plane strain compression*

For the case of plane strain compression, an aggregate of 400 grains is represented by 400 square two-dimensional ABAQUS-CPE4 (continuum, plane-strain, four-noded) elements. (These elements address the problem of mesh-locking in (near) incompressible situations by using the method of Nagtegaal *et al.* (1974).) A set of 400 initially 'random' grain orientations were assigned to the elements. Figure 18*a* shows the initial mesh geometry for plane strain compression. It is important to note that even though the geometry is chosen to be two-dimensional, the model incorporates the full three-dimensional slip system structure. The top and bottom planes of the specimen were constrained to remain plane, modelled as being free from shear tractions, and subjected to displacement boundary conditions which resulted in an axial true strain rate of $-0.001\ \mathrm{s}^{-1}$. The deformed finite element mesh at

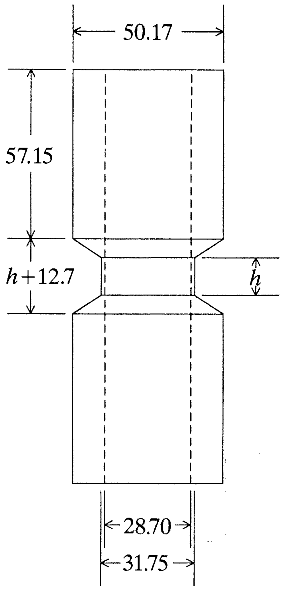

Figure 13. Thin-walled tubular torsion specimen. Dimensions are in millimetres.

$\epsilon = -1.0$ is shown in figure 18*b*. Since the sides of the finite element mesh are unconstrained, one once again obtains the 'orange peel' effect. The calculation had to be terminated when the grains became too distorted.

Figure 19 shows the experimental and calculated stress–strain curves. The stress–strain response from the finite element calculation is softer than that from the Taylor model calculation and neither the Taylor model nor the finite element model capture the decrease in the slope of the stress–strain curve associated with shear localization.

Figure 20 shows a comparison of the evolved {111} pole figures after an axial compressive strain of -1.0. The finite-element calculated texture is in much better agreement with the experimental texture as compared to the Taylor model prediction. In particular, note that the finite element simulations capture the diffuse dumbbell like shape in the experimental {111} pole figure, whereas in the texture predicted by the Taylor model exhibits a sharp elliptical shape.

(iii) *Simple shear*

In this calculation an aggregate of 400 crystals is represented by 400 square two-dimensional CPE4 ABAQUS elements and this array is subjected to a simple shear deformation as shown in figure 21. The stress–strain response for simple shear predicted by this procedure is also shown in figure 11. The predictions of the normal stress from the finite element model are in much better agreement with the experiments than the predictions from the Taylor model.

Figure 22 shows a comparison of the evolved texture after a shear strain of -1.40. The experimental pole figure is the one measured from the planar double shear experiment. Again, the texture predicted by the Taylor model is sharper than that predicted by both the finite element model and the experimental result.

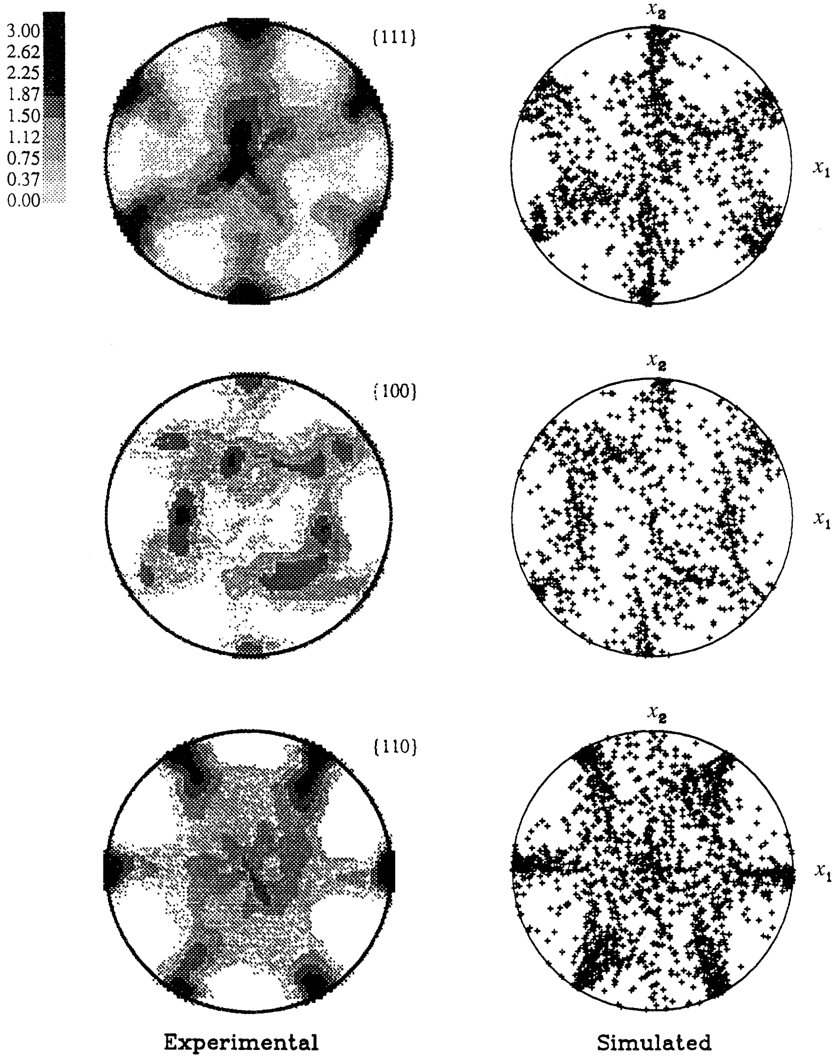

Figure 14. Experimental and simulated crystallographic texture for thin wall tube torsion to $\gamma_{12} = -1.50$.

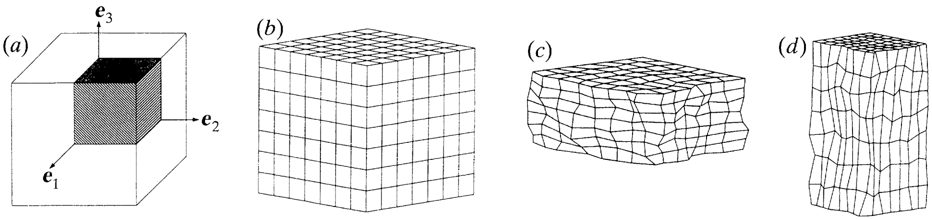

Figure 15. Initial and deformed finite element meshes for ‘simple’ compression and tension simulations.

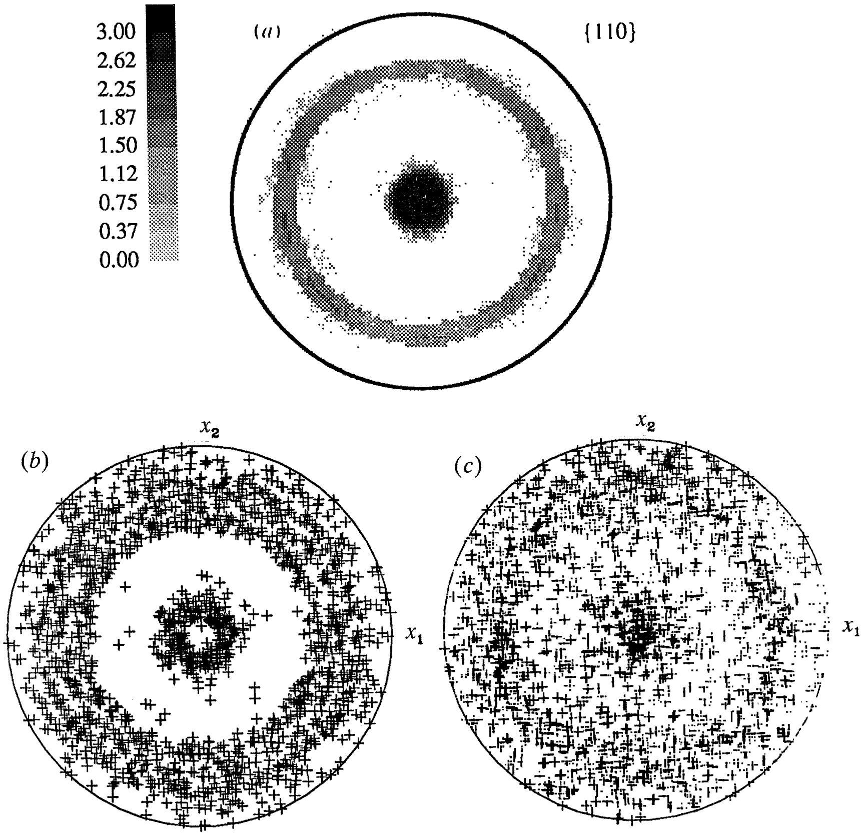

Figure 16. {110} pole figures after compression to $\epsilon_{33} = -1.00$. (*a*) Experimental. (*b*) Taylor model calculation using crystals with the same initial orientations as those used for the finite element calculation. (*c*) Finite element calculation.

6. Conclusion

A generalized Taylor-type polycrystal constitutive model together with an implicit time-integration scheme have been developed to calculate the stress–strain response and to describe the evolution of crystallographic texture during large deformations of FCC metals. The constitutive model is evaluated by comparing the predictions for the evolution of texture and the stress–strain curves in simple compression and tension, plane strain compression, and simple shear of initially 'isotropic' OFHC copper against (*a*) corresponding experiments, and (*b*) finite element simulations of these experiments using a multitude of single crystals with accounting (in the 'weak' sense) for the satisfaction of both compatibility and equilibrium.

We agree with Leffers *et al.* (1988) who in a recent panel report wrote that the 'Taylor model is a reasonably good first approximation for the texture formation and the anisotropy, at least in single-phase materials'. Our experiments and calculations show that the Taylor-type model is in reasonable first-order agreement with the experiments for the texture formation and also the overall stress–strain response of single-phase copper. The results of the finite element calculations are in much better agreement with experiments, but at a substantially higher computational expense.

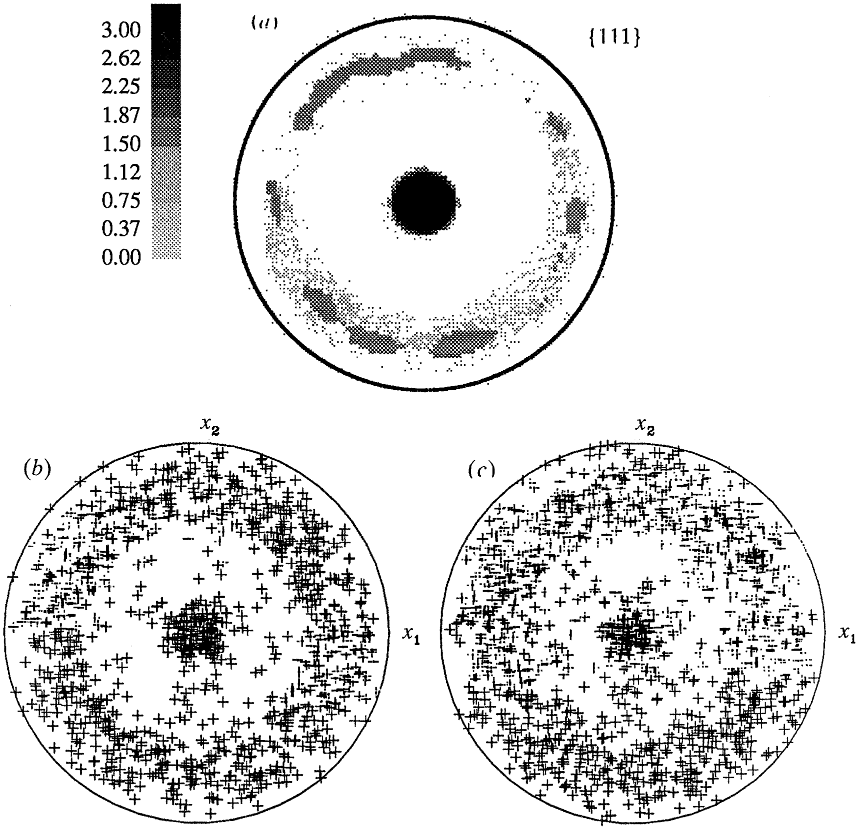

Figure 17. {111} pole figures after tension to $\epsilon_{33} = 0.37$. (*a*) Experimental. (*b*) Taylor model calculation using crystals with the same initial orientations as those used for the finite element calculation. (*c*) Finite element calculation.

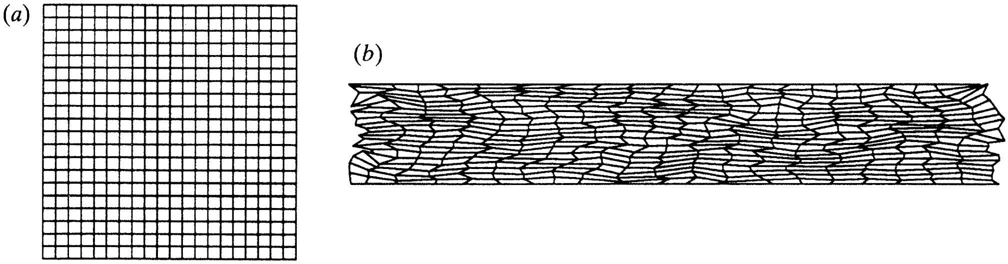

Figure 18. Finite element mesh for the plane strain compression calculation: (*a*) undeformed mesh, and (*b*) deformed mesh at an axial compressive strain of -1.0.

The support of the Solid Mechanics Program of the U.S. Office of Naval Research under grant ONR no. 0014-J-3040 is gratefully acknowledged.

Appendix A. Time integration procedure

Let τ denote a time Δt later than time t, the time-integration problem for the Taylor-type model may be stated as follows.

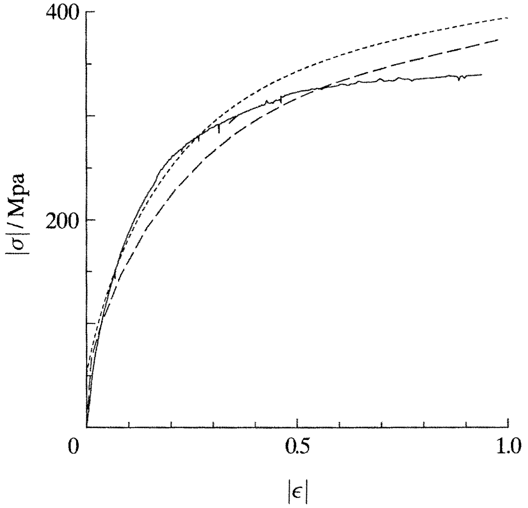

Figure 19. ——, Experimental; ----, Taylor model; — — — —, finite element model: axial stress against logarithmic axial strain response for plane strain compression.

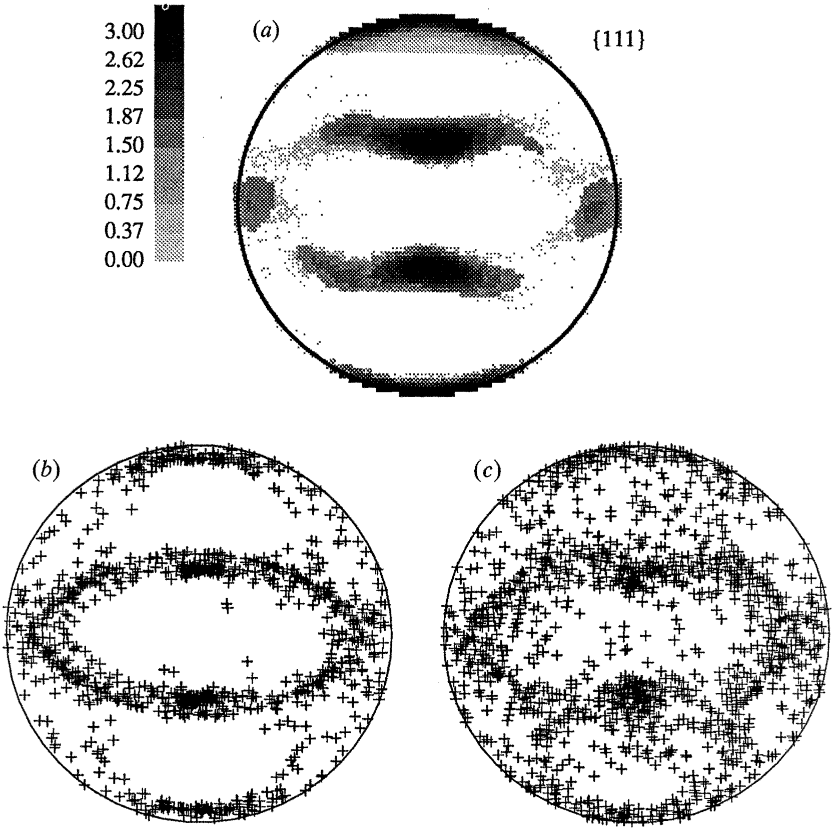

Figure 20. {111} pole figures after plane strain compression to $\epsilon_{33} = -1.0$. (*a*) Experimental. (*b*) Taylor model calculation using crystals with the same initial orientations as those used for the finite element calculation. (*c*) Finite element calculation.

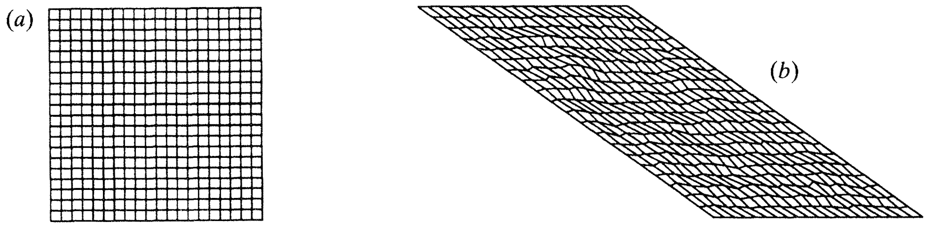

Figure 21. Finite element mesh for the simple shear calculation: (*a*) undeformed mesh and (*b*) deformed mesh at a shear strain of −1.4.

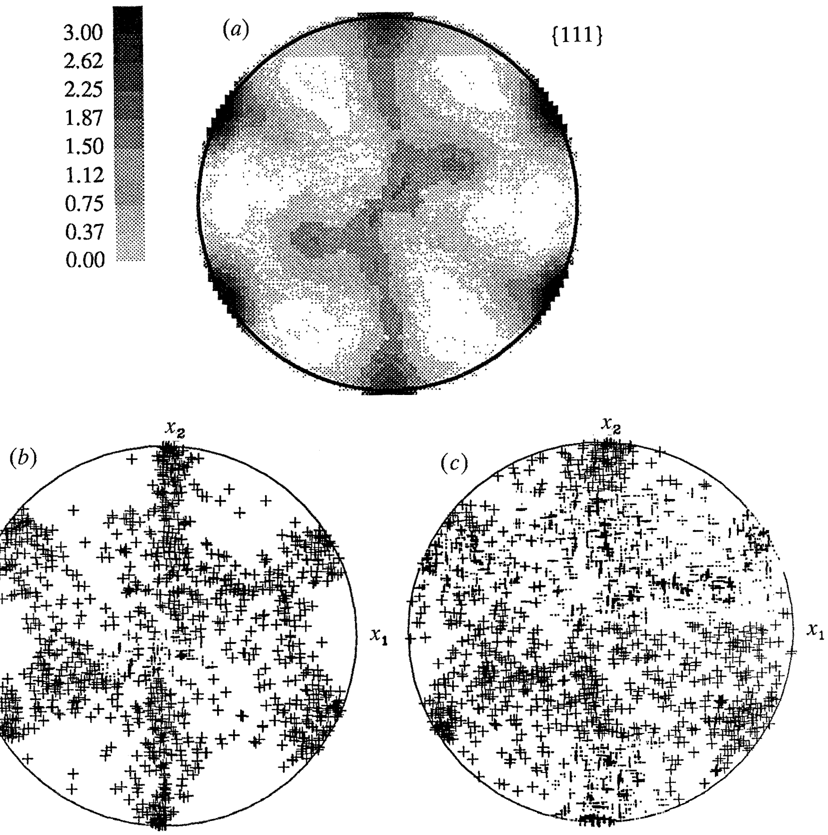

Figure 22. {111} pole figures after simple shear to $\gamma = -1.4$. (*a*) Experimental. (*b*) Taylor model calculation using crystals with the same initial orientations as those used for the finite element calculation. (*c*) Finite element calculation.

Given: (1) $\boldsymbol{F}(t)$, $\boldsymbol{F}(\tau)$; (2) $(\boldsymbol{m}_0^\alpha, \boldsymbol{n}_0^\alpha)$ – time-independent quantities, for each grain; (3) $\{\boldsymbol{F}^{\mathrm{p}}(t), s^\alpha(t), \boldsymbol{T}(t)\}$ in each grain.

Calculate: (*a*) $\{\boldsymbol{F}^{\mathrm{p}}(\tau), s^\alpha(\tau), \boldsymbol{T}(\tau)\}$ for each grain; (*b*) the volume averaged macroscopic stress

$$\bar{\boldsymbol{T}} = \frac{1}{N}\sum_{k=1}^{N} \boldsymbol{T}^{(k)};$$

(*c*) texture at time τ from

$$\boldsymbol{m}^\alpha_\tau = \boldsymbol{F}^*(\tau)\,\boldsymbol{m}^\alpha_0 = \boldsymbol{F}(\tau)\,\boldsymbol{F}^{\mathrm{p}-1}(\tau)\,\boldsymbol{m}^\alpha_0,$$
$$\boldsymbol{n}^\alpha_\tau = \boldsymbol{F}^{*-\mathrm{T}}(\tau)\,\boldsymbol{n}^\alpha_0 = \boldsymbol{F}^{-\mathrm{T}}(\tau)\,\boldsymbol{F}^{\mathrm{pT}}(\tau)\,\boldsymbol{n}^\alpha_0,$$

and march forward in time.

After calculating the list of quantities in part (*a*) of the problem, parts (*b*) and (*c*) are self-explanatory and straightforward. The solution procedure for part (*a*) has been detailed in Kalidindi *et al.* (1992). The steps in this procedure are:

(i) Compute

$$\boldsymbol{A} \equiv \boldsymbol{F}^{\mathrm{p}-\mathrm{T}}(t)\,\boldsymbol{F}^{\mathrm{T}}(\tau)\,\boldsymbol{F}(\tau)\,\boldsymbol{F}^{\mathrm{p}-1}(t), \tag{A 1}$$

$$\boldsymbol{T}^{*\mathrm{tr}} \equiv \mathscr{L}\left[\tfrac{1}{2}\{\boldsymbol{A}-\boldsymbol{1}\}\right], \tag{A 2}$$

$$\boldsymbol{B}^\alpha \equiv \boldsymbol{A}\boldsymbol{S}^\alpha_0 + \boldsymbol{S}^{\alpha\mathrm{T}}_0\boldsymbol{A}, \tag{A 3}$$

$$\boldsymbol{C}^\alpha \equiv \mathscr{L}\left[\tfrac{1}{2}\boldsymbol{B}^\alpha\right]. \tag{A 4}$$

(ii) Solve

$$\boldsymbol{T}^*(\tau) \doteq \boldsymbol{T}^{*\mathrm{tr}} - \sum_\alpha \Delta\gamma^\alpha \boldsymbol{C}^\alpha, \tag{A 5}$$

$$s^\alpha(\tau) = s^\alpha(t) + \sum_\beta h^{\alpha\beta}(\tau)\,|\Delta\gamma^\beta|, \tag{A 6}$$

with

$$\Delta\gamma^\alpha \equiv \dot{\gamma}^\alpha(\tau)\,\Delta t, \tag{A 7}$$

for $\boldsymbol{T}^*(\tau)$ and $s^\alpha(\tau)$ using the following two-level iterative procedure.

In the first level of iterations, solve equation (A 5) for $\boldsymbol{T}^*(\tau)$, keeping $s^\alpha(\tau)$ fixed at its best available estimate, by using a Newton-type iterative algorithm as follows:

$$\boldsymbol{T}^*_{n+1}(\tau) = \boldsymbol{T}^*_n(\tau) - \mathscr{J}_n^{-1}[\boldsymbol{G}_n], \tag{A 8}$$

with

$$\boldsymbol{G}_n \equiv \boldsymbol{T}^*_n(\tau) - \boldsymbol{T}^{*\mathrm{tr}} + \sum_\alpha \Delta\gamma^\alpha(\boldsymbol{T}^*_n(\tau), s^\alpha_k(\tau))\,\boldsymbol{C}^\alpha, \tag{A 9}$$

$$\mathscr{J}_n \equiv \mathscr{I} + \sum_\alpha \boldsymbol{C}^\alpha \otimes \frac{\partial}{\partial \boldsymbol{T}^*_n(\tau)}\Delta\gamma^\alpha(\boldsymbol{T}^*_n(\tau), s^\alpha_k(\tau)), \tag{A 10}$$

where $\mathscr{J}_n = \partial\boldsymbol{G}_n/\tilde{\partial}\boldsymbol{T}^*_n(\tau)$ at fixed $s^\alpha_k(\tau)$. In the equations above, the subscripts n and $n+1$ refer to estimates of $\boldsymbol{T}^*(\tau)$ at the end of n and $n+1$ iterations respectively, in the first level of the iterative scheme. The second level of the iterative procedure involves a simple update (without iterations) of $s^\alpha(\tau)$ using

$$s^\alpha_{k+1} = s^\alpha(t) + \sum_\beta h^{\alpha\beta}(s^\beta_k(\tau))\,|\Delta\gamma^\beta(\boldsymbol{T}^*_{n+1}(\tau), s^\beta_k(\tau))|, \tag{A 11}$$

where the subscript k refers to the value of $s^\alpha(\tau)$ at the end of the kth update in the second level of the iterative scheme.

For low rate sensitivity of plastic flow, the set of equations (A 5) is very stiff and it becomes necessary to apply constraints to the Newton corrections (equations (A 8)) in the first level of the iterative procedure. In our calculations, the following constraint has been used. Let

$$\Delta T^*_{ij} \equiv (T^*_{ij})_{n+1}(\tau) - (T^*_{ij})_n(\tau), \tag{A 12}$$

denote the increments in the values of the components of $\boldsymbol{T}^*(\tau)$ calculated by the

Newton procedure in an iteration. If $|\Delta T^*_{ij}| < \eta s_o$, then accept the Newton correction, else

$$(T^*_{ij})_{n+1}(\tau) = (T^*_{ij})_n(\tau) + \eta s_o \operatorname{sgn}\{\Delta T^*_{ij}\}, \tag{A 13}$$

where s_o denotes the initial value of the slip system resistance and η is a numerical constant. A value of η of 0.67 was found to give good results for our calculations.

(iii) Compute

$$\boldsymbol{F}^{\mathrm{p}}(\tau) \doteq \left\{1 + \sum_{\alpha} \Delta\gamma^{\alpha} \boldsymbol{S}^{\alpha}_{0}\right\} \boldsymbol{F}^{\mathrm{p}}(t). \tag{A 14}$$

Normalize $\boldsymbol{F}^{\mathrm{p}}(\tau)$ by dividing the computed values of each of its components by the cube root of the computed determinant. This normalization procedure ensures that the determinant of $\boldsymbol{F}^{\mathrm{p}}(\tau)$ is unity.

(iv) Finally, compute

$$\boldsymbol{T}(\tau) = \frac{1}{\det \boldsymbol{F}(\tau)} \boldsymbol{F}(\tau)\, \boldsymbol{F}^{\mathrm{p}-1}(\tau)\, \boldsymbol{T}^*(\tau)\, \boldsymbol{F}^{\mathrm{p}-\mathrm{T}}(\tau)\, \boldsymbol{F}^{\mathrm{T}}(\tau). \tag{A 15}$$

References

Abaqus 1990 *Reference manuals*. Providence: Hibbitt, Karlsson and Sorensen Inc.

Anand, L. 1985 Constitutive equations for hot-working of metals. *Int. J. Plast.* **1**, 213–231.

Asaro, R. J. 1983*a* Micromechanics of crystals and polycrystals. *Adv. appl. Mech.* **23**, 1–115.

Asaro, R. J. 1983*b* Crystal plasticity. *J. appl. Mech. Trans. ASME* **50**, 921–934.

Asaro, R. J. & Needleman, A. 1985 Texture development and strain hardening in rate dependent polycrystals. *Acta metall.* **33**, 923–953.

Asaro, R. J. & Rice, J. R. 1977 Strain localization in ductile single crystals. *J. Mech. Phys. Solids* **25**, 309–338.

Bronkhorst, C. A. 1991 Ph.D. thesis, Massachusetts Institute of Technology.

Brown, S. B., Kim, K. H. & Anand, L. 1989 An internal variable constitutive model for hot working of metals. *Int. J. Plast.* **5**, 95–130.

Gil-Sevillano, J., van Houtte, P. & Aernoudt, E. 1980 Large strain work hardening and textures. *Prog. mater. Sci.* **25**, 69–412.

Gurtin, M. E. 1981 *An introduction to continuum mechanics*. New York: Academic Press.

Harren, S. V. & Asaro, R. J. 1989 Nonuniform deformations in polycrystals and aspects of the validity of the Taylor model. *J. Mech. Phys. Solids* **37**, 191–232.

Harren, S. V., Lowe, T. C., Asaro, R. J. & Needleman, A. 1989 Analysis of large-strain shear in rate-dependent face-centred cubic polycrystals: correlations of micro- and macromechanics. *Phil. Trans. R. Soc. Lond.* A **328**, 443–500.

Hill, R. & Rice, J. R. 1972 Constitutive analysis of elastic-plastic crystals at arbitrary strain. *J. Mech. Phys. Solids* **20**, 401–413.

Hirsch, J., Lücke, K. & Hatherly, M. 1988 Mechanism of deformation and development of rolling textures in polycrystalline FCC metals. III. The influence of slip inhomogeneities and twinning. *Acta metall.* **36**, 2905–2927.

Hutchinson, J. W. 1976 Bounds and self-consistent estimates for creep of polycrystalline materials. *Proc. R. Soc. Lond.* A **348**, 101–127.

Kalidindi, S. R., Bronkhorst, C. A. & Anand, L. 1992 Crystallographic texture evolution in bulk deformation processing of FCC metals. *J. Mech. Phys. Solids* **40**, 537–579.

Kallend, J. S., Kocks, U. F., Rollett, A. D. & Wenk, H.-R. 1989 *popLA: the preferred orientation package from Los Alamos*.

Leffers, T., Asaro, R. J., Driver, J. H., Kocks, U. F., Mecking, H., Tomé, C. & van Houtte, P. 1988 *Proceedings of the Eighth International Conference on Textures of Materials*, pp. 265–272.

Taylor, G. I. 1938 Plastic strain in metals. *J. Inst. Metals* **62**, 307–324.

Nagtegaal, J., Parks, D. M. & Rice, J. R. 1974 On numerically accurate finite element solutions in the fully plastic range. *Int. J. Solids Struct.* **11**, 601–616.

Rice, J. R. 1971 Inelastic constitutive relations for solids: an internal variable theory and its application to metal plasticity. *J. Mech. Phys. Solids* **19**, 433–455.

Weber, G. & Anand, L. 1990 Finite deformation constitutive equations and a time integration procedure for isotropic, hyperelastic-viscoplastic solids. *Comp. Methods appl. Mech. Engng* **79**, 173–202.

Wenk, H.-R. 1985 Preferred orientation in deformed metals and rocks: an introduction to modern texture analysis. Orlando: Academic Press.

Williams, R. O. 1962 Shear textures in copper, brass, aluminum, iron, and zirconium. *Trans. Met. Soc. AIME* **224**, 129–140.

Received 11 March 1991; revised 6 January 1992; accepted 18 March 1992

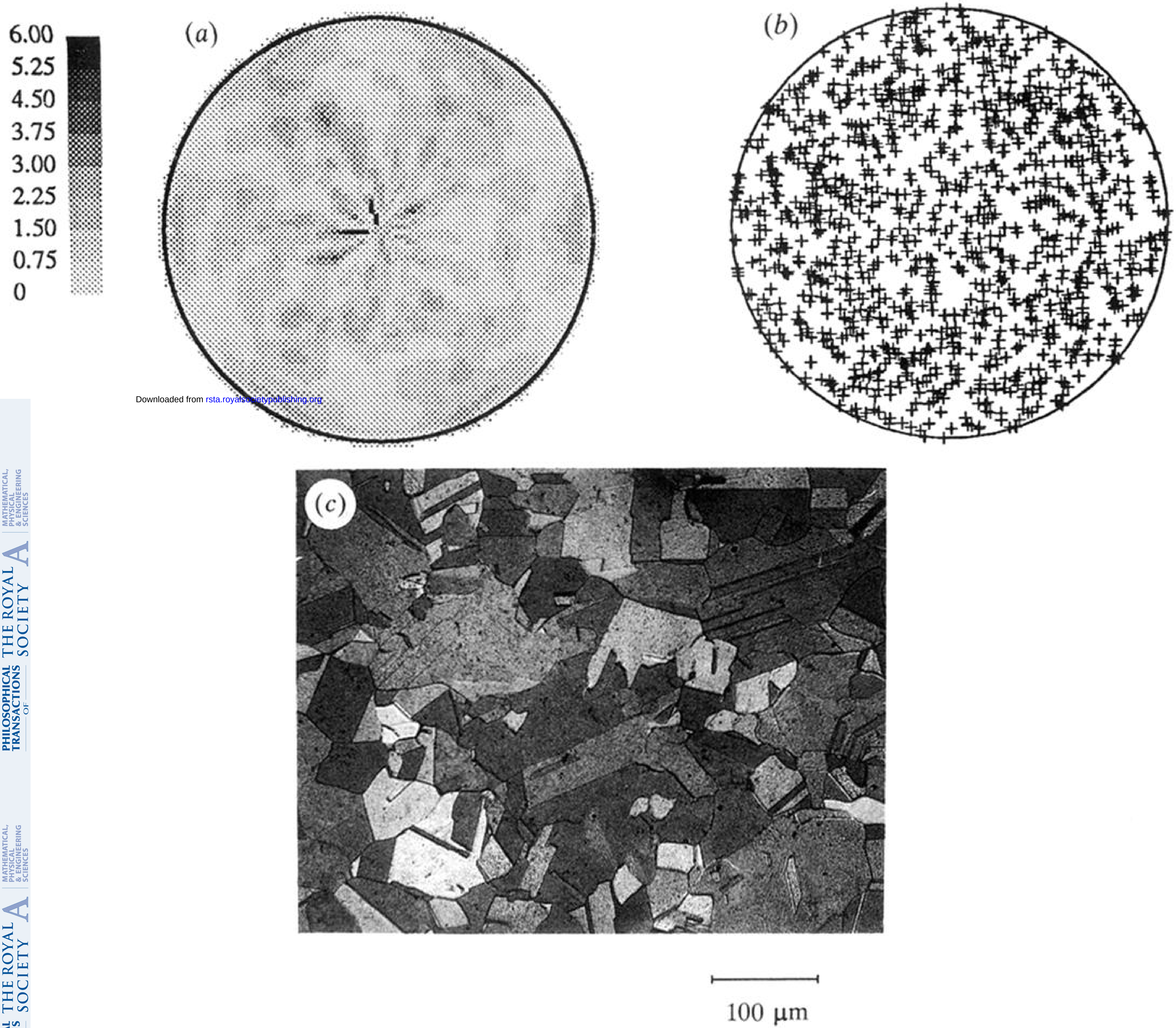

igure 1. (*a*) Initial experimental {111} (equal area projection) pole figure of annealed OFHC copper.) Representation of initial 'isotropic' texture by 300 crystals. (*c*) Photomicrograph of annealed opper.

PHILOSOPHICAL TRANSACTIONS OF THE ROYAL SOCIETY A MATHEMATICAL, PHYSICAL & ENGINEERING SCIENCES

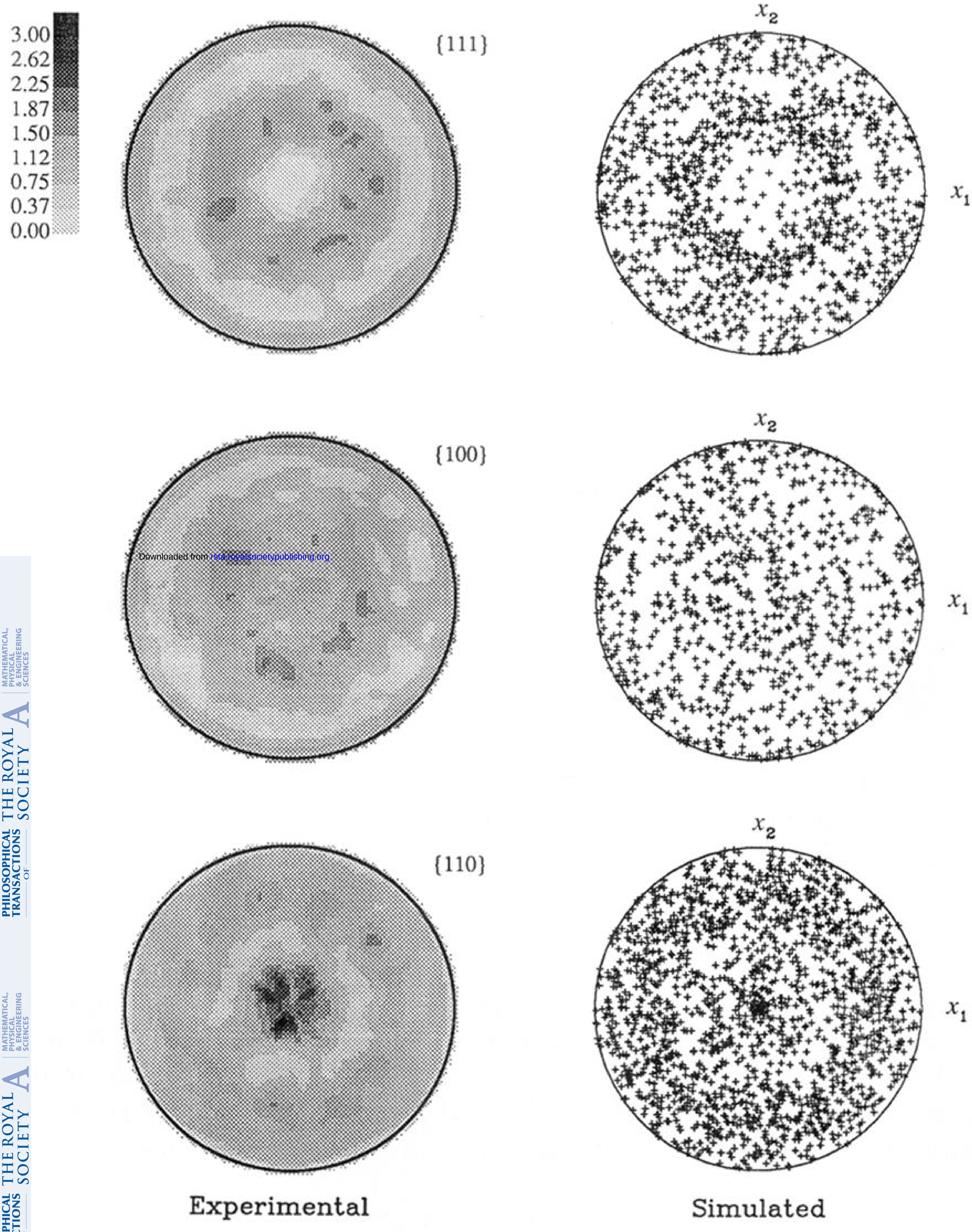

Figure 3(*a*). Experimental and simulated crystallographic texture for simple compression to $\epsilon_{33} = -0.20$.

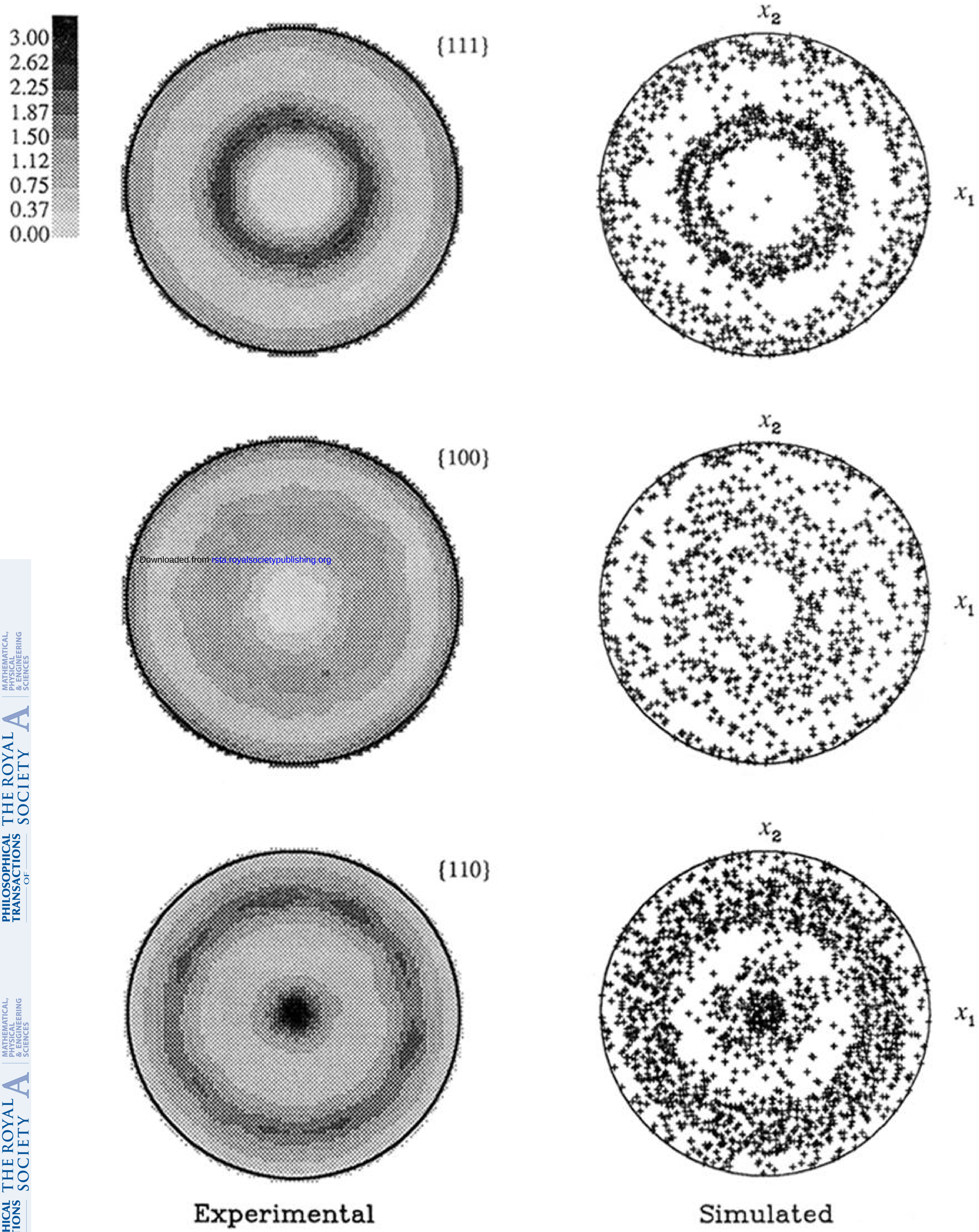

Figure 3(*b*). Experimental and simulated crystallographic texture for simple compression to $\epsilon_{33} = -0.49$.

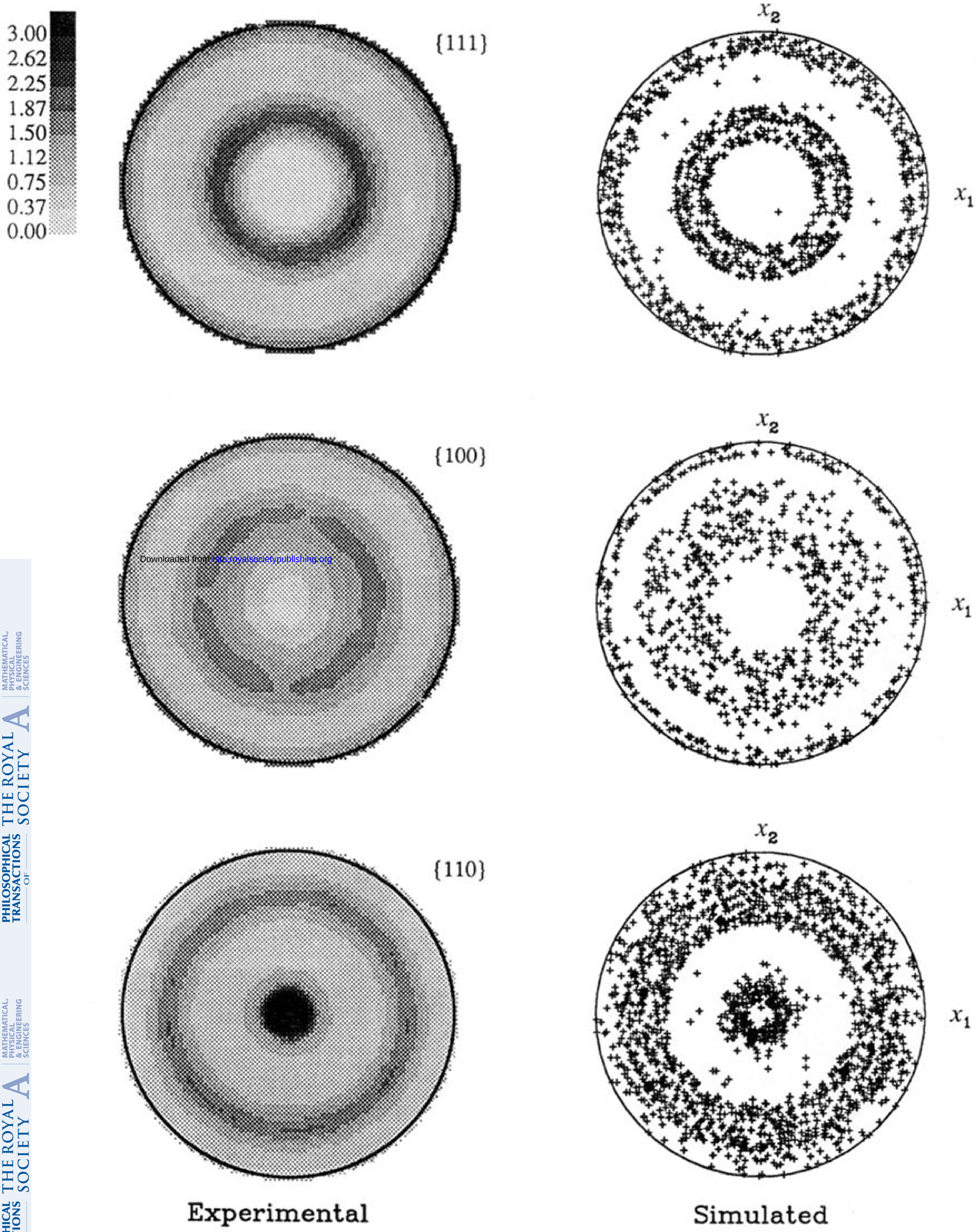

Figure 3(*c*). Experimental and simulated crystallographic texture for simple compression to $\epsilon_{33} = -0.99$.

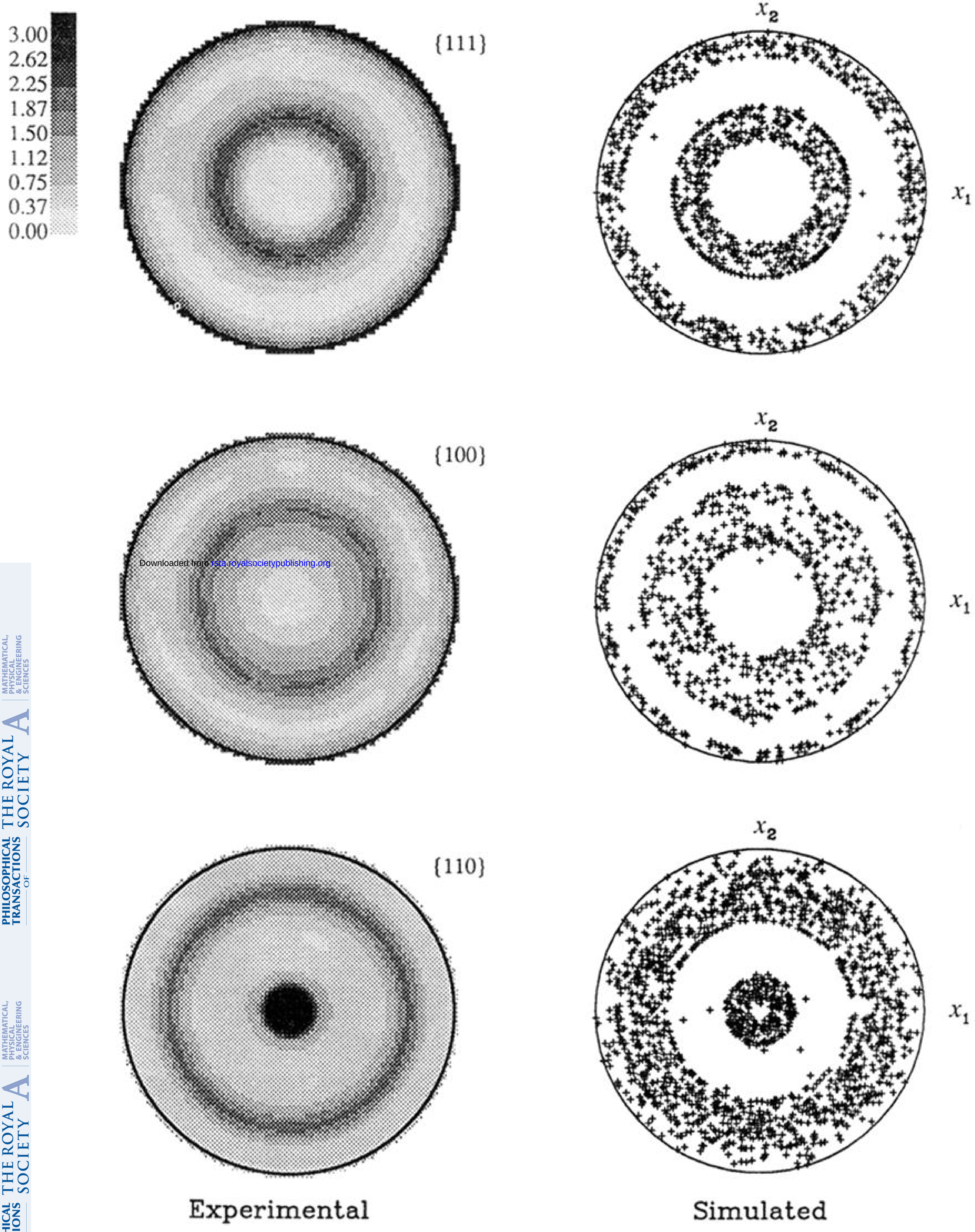

Figure 3(*d*). Experimental and simulated crystallographic texture for simple compression to $\epsilon_{33} = -1.53$.

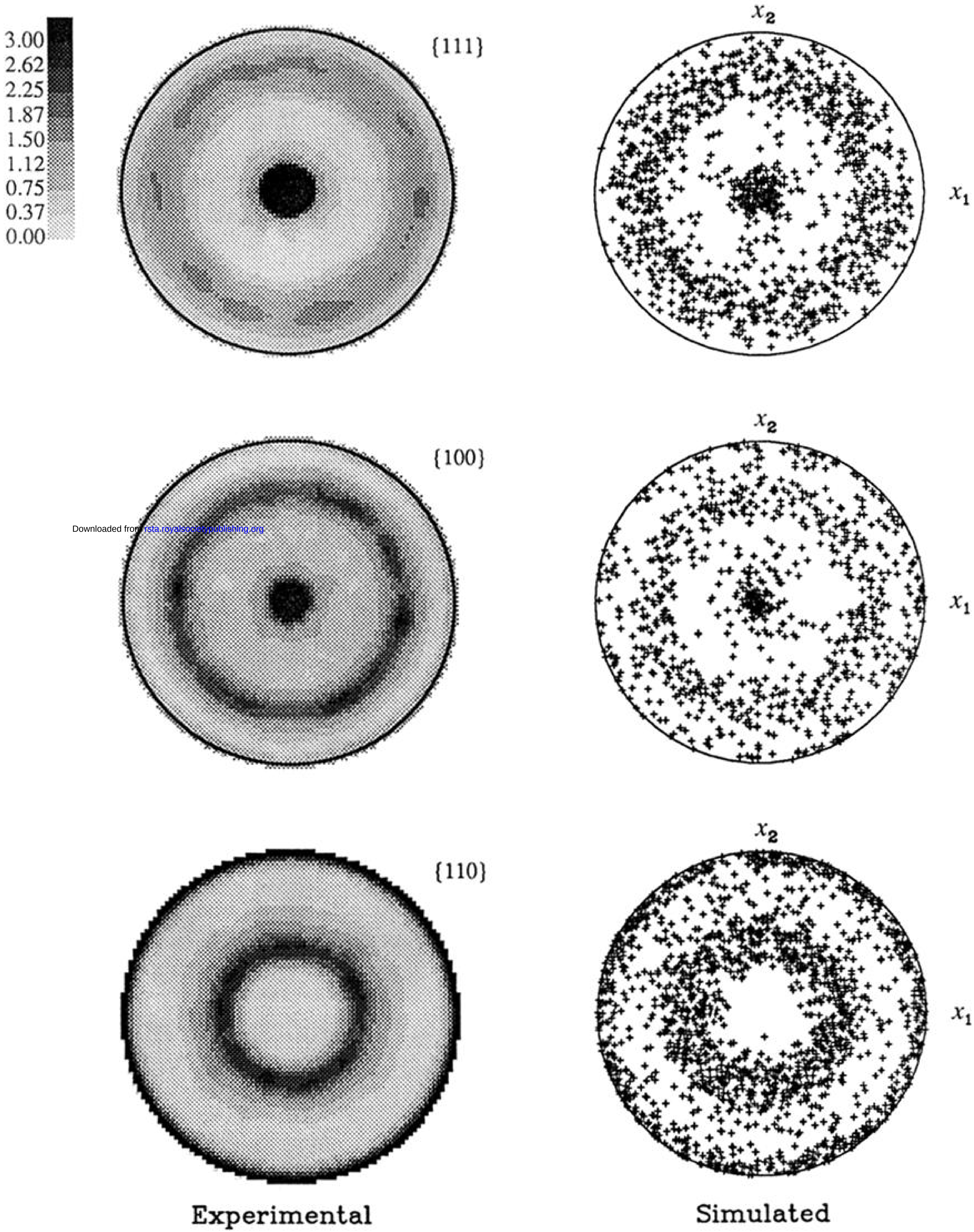

gure 6. Experimental and simulated crystallographic texture for simple tension to $\epsilon_{33} = 0.37$.

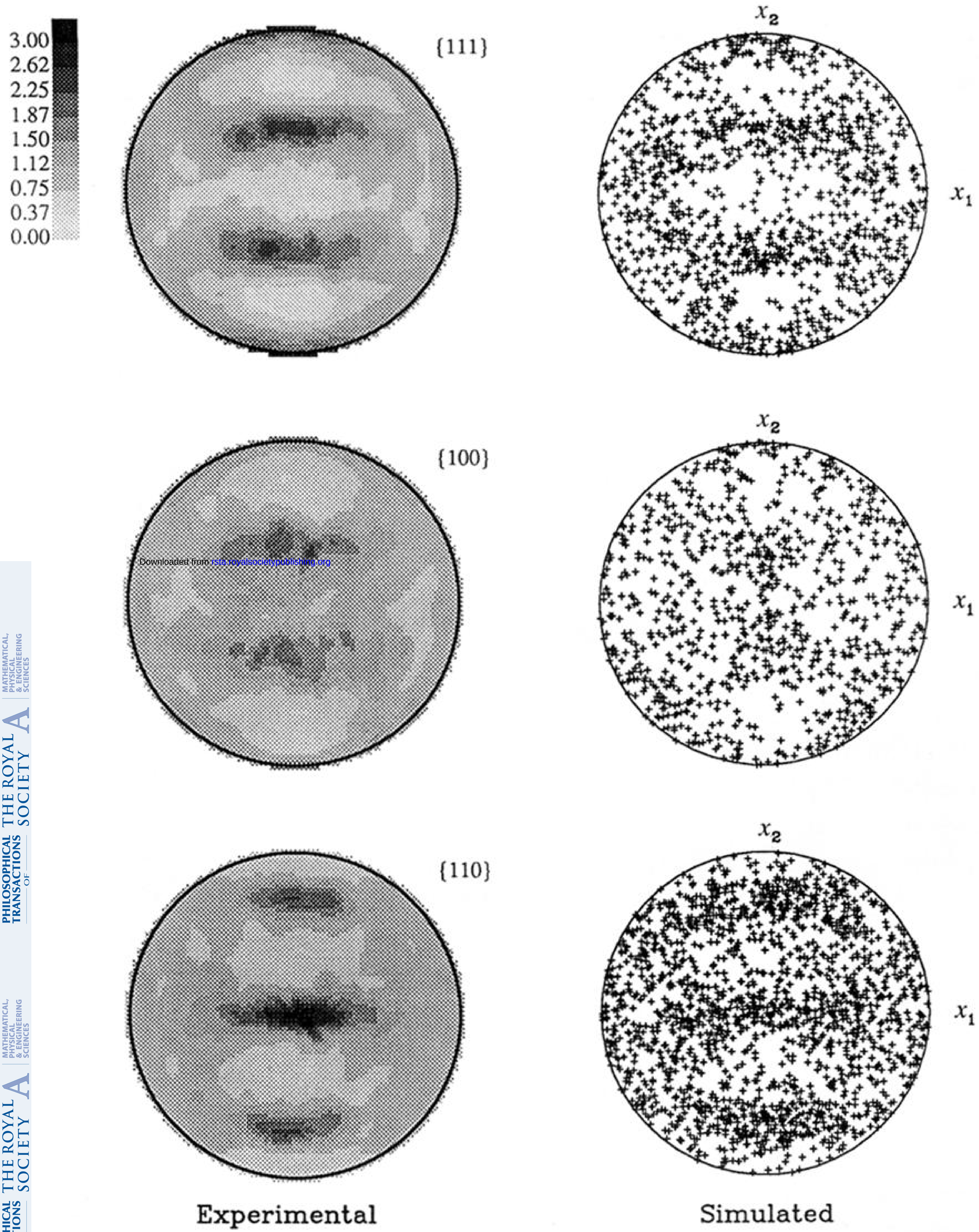

Figure 8 (*a*). Experimental and simulated crystallographic texture for plane strain compression to $\epsilon_{33} = -0.21$.

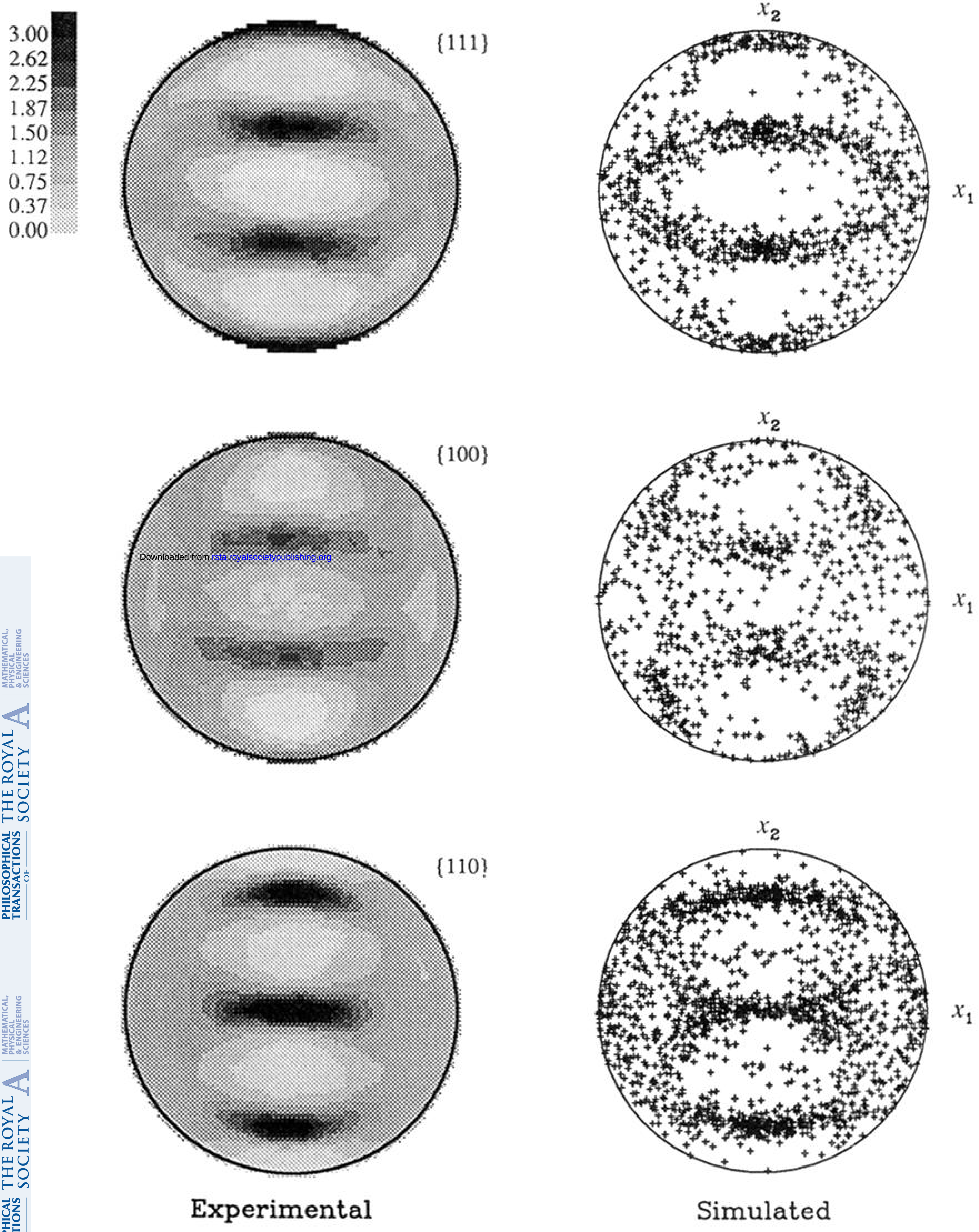

Figure 8(b). Experimental and simulated crystallographic texture for plane strain compression to $\epsilon_{33} = -0.52$.

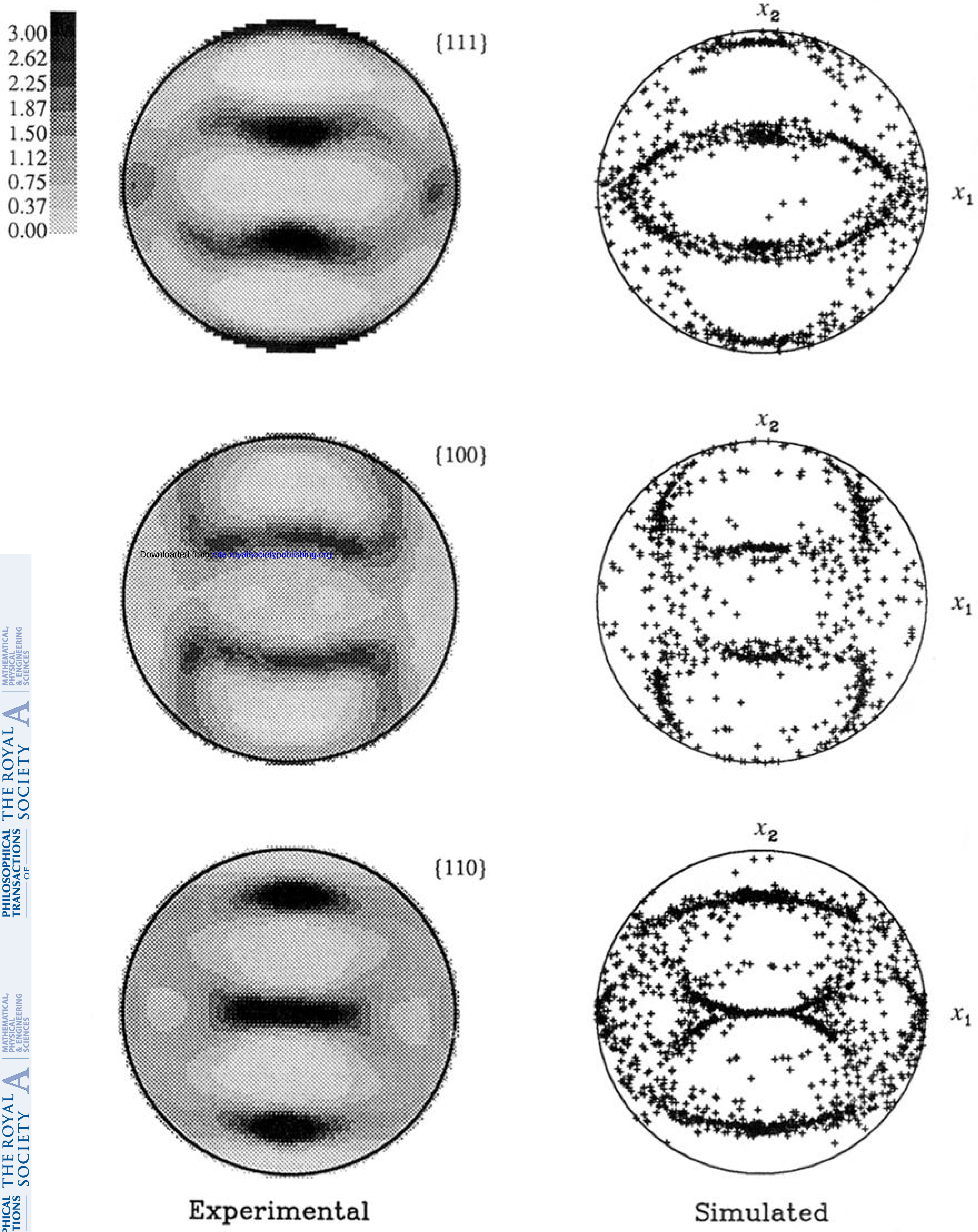

Figure 8(*c*). Experimental and simulated crystallographic texture for plane strain compression to $\epsilon_{33} = -1.01$.

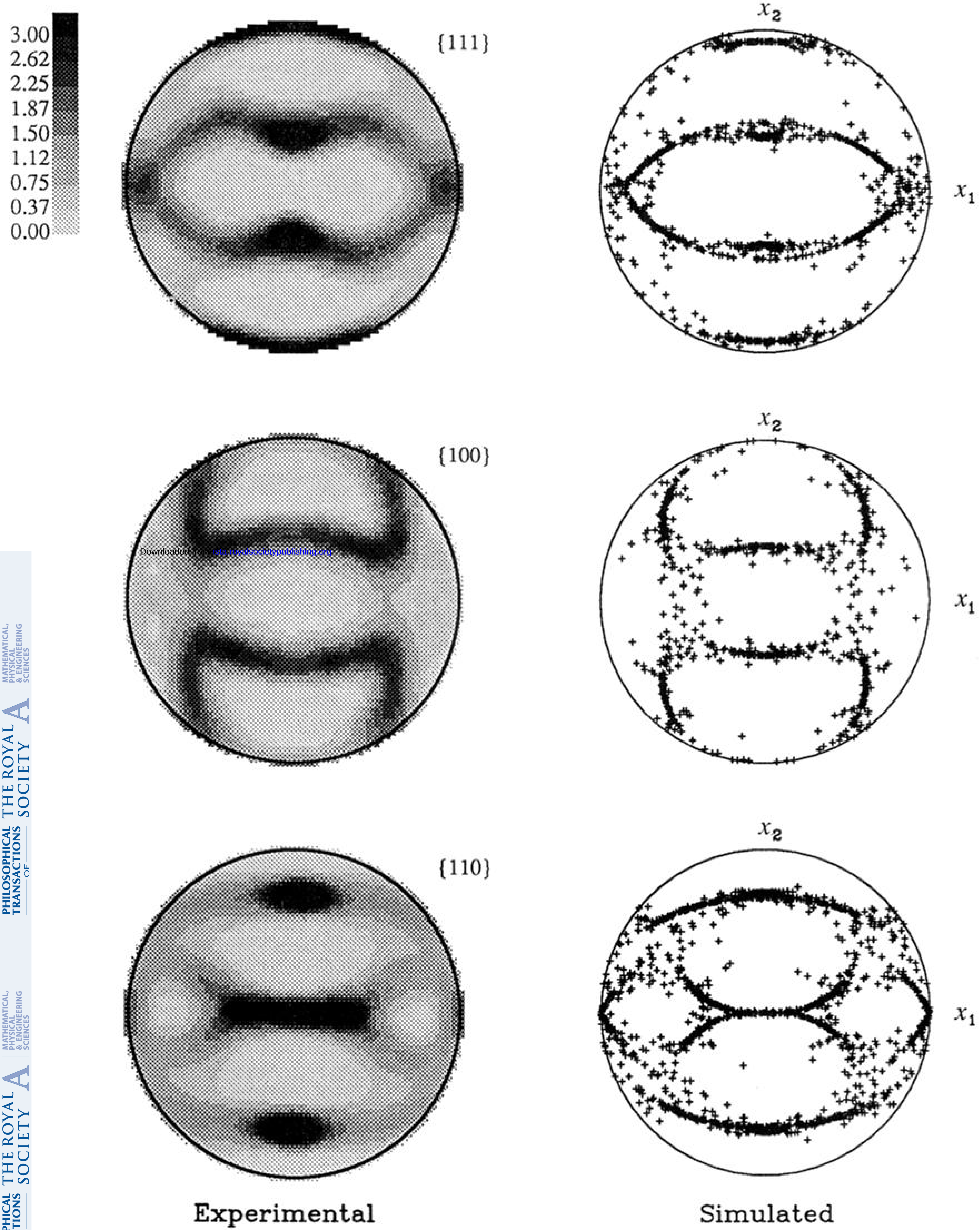

Figure 8(*d*). Experimental and simulated crystallographic texture for plane strain compression to $\epsilon_{33} = 1.54$.

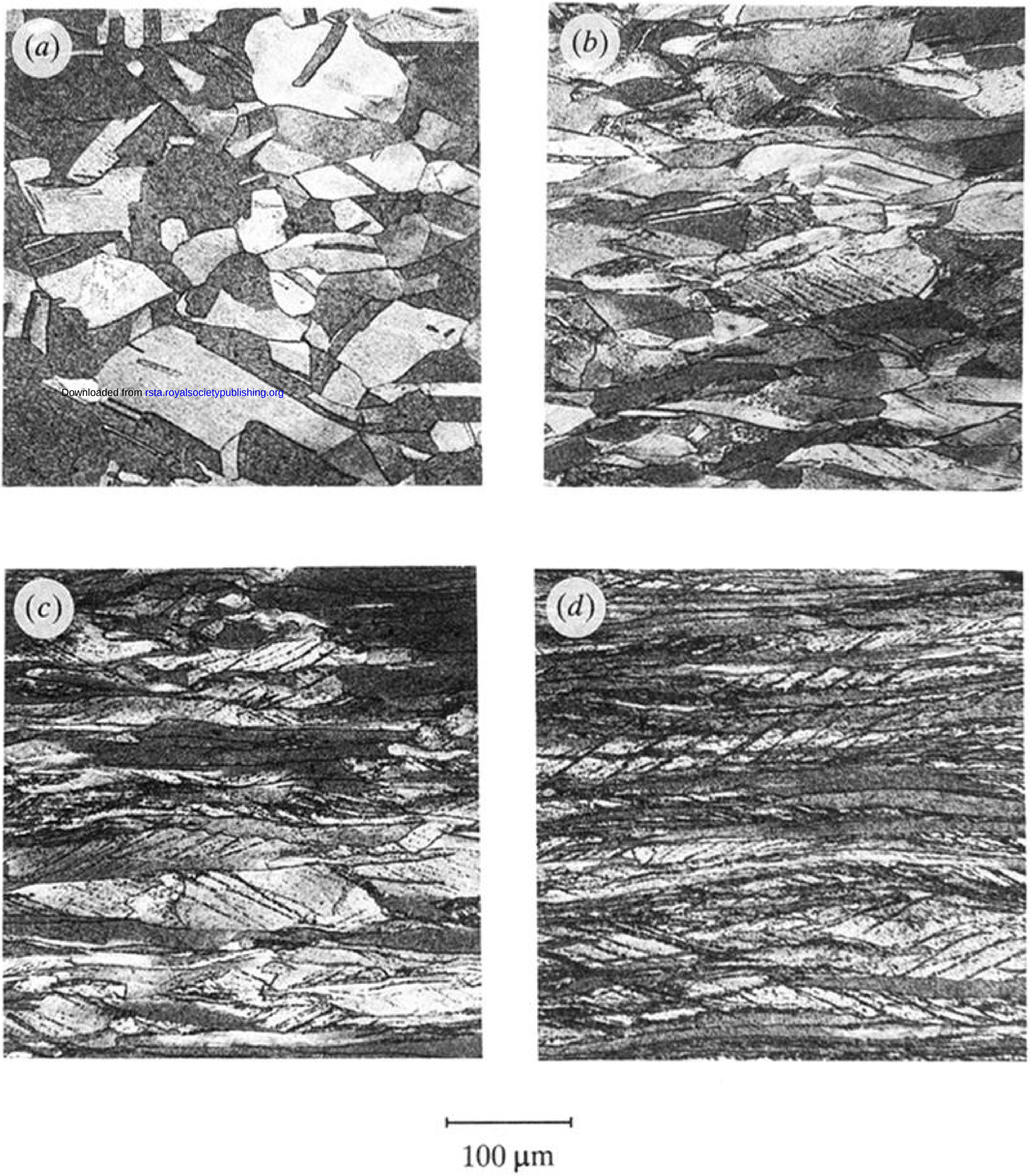

gure 9. Photo-micrographs of OFHC copper deformed by plane strain compression: (a) $\epsilon_{33} = -0.21$; (b) $\epsilon_{33} = -0.52$; (c) $\epsilon_{33} = -0.1$; (d) $\epsilon_{33} = -1.54$.

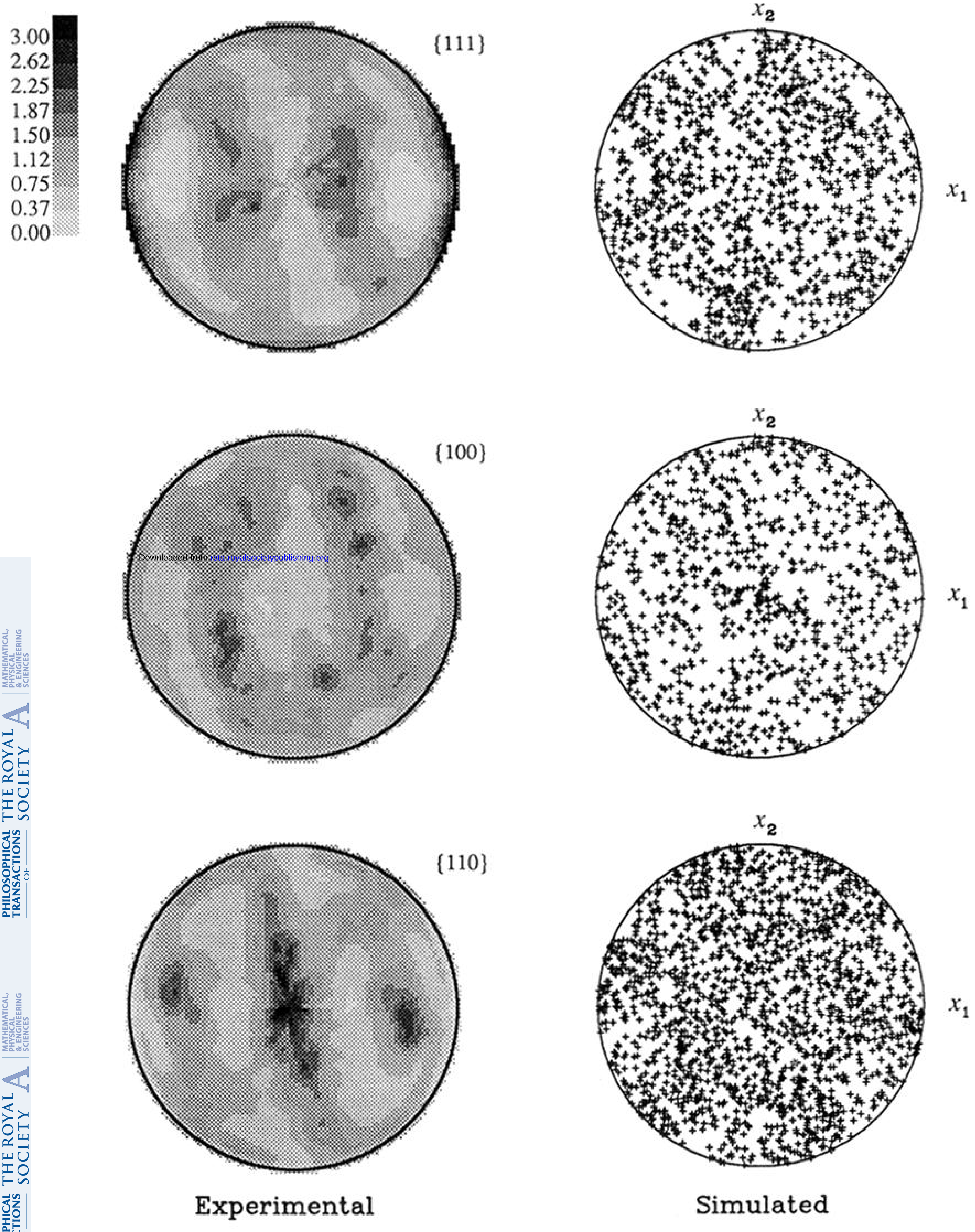

Figure 12(*a*). Experimental and simulated crystallographic texture for planar simple shear to $\gamma_{12} = -0.26$.

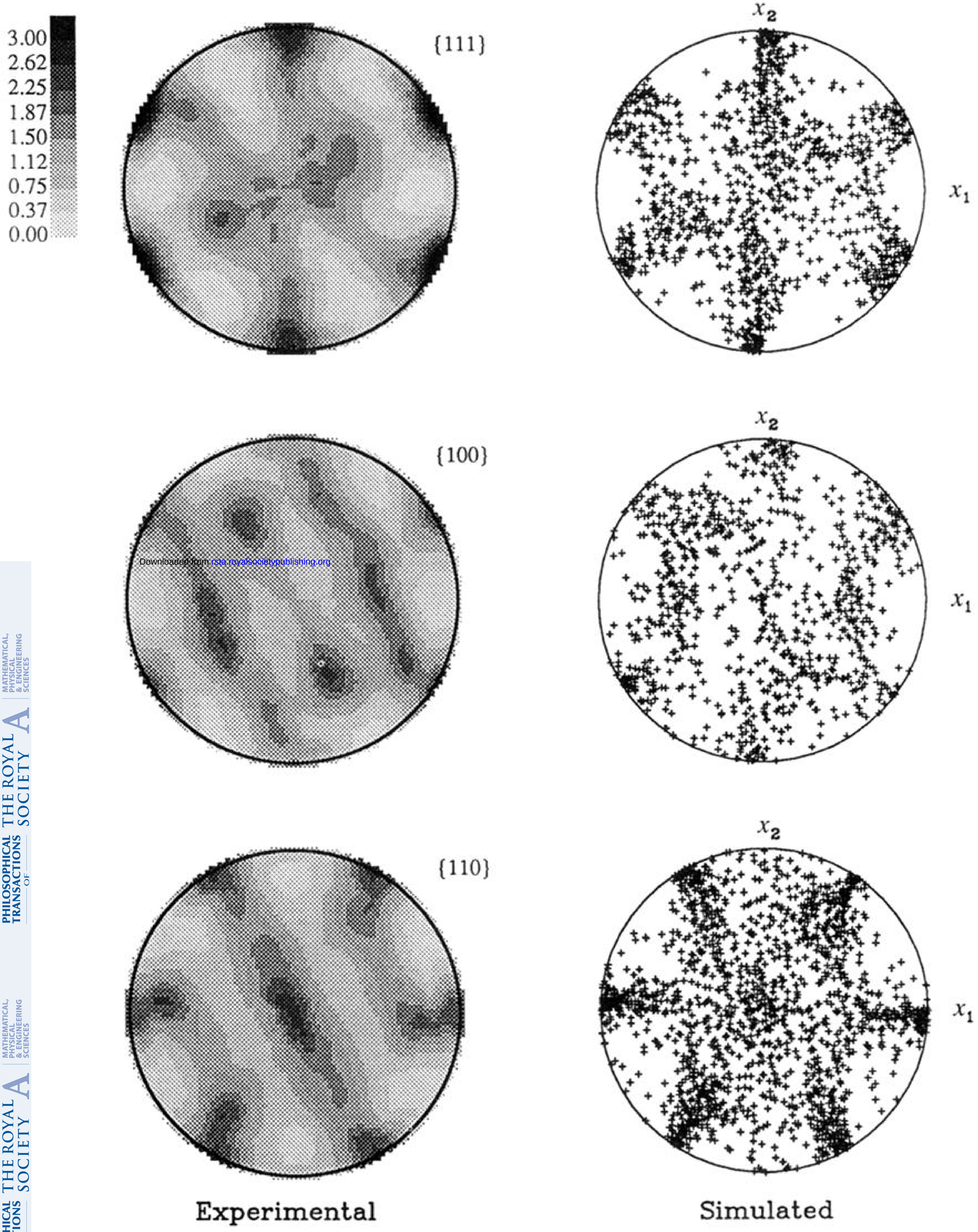

Figure 12 (*b*). Experimental and simulated crystallographic texture for planar simple shear to $\gamma_{12} = -0.43$.

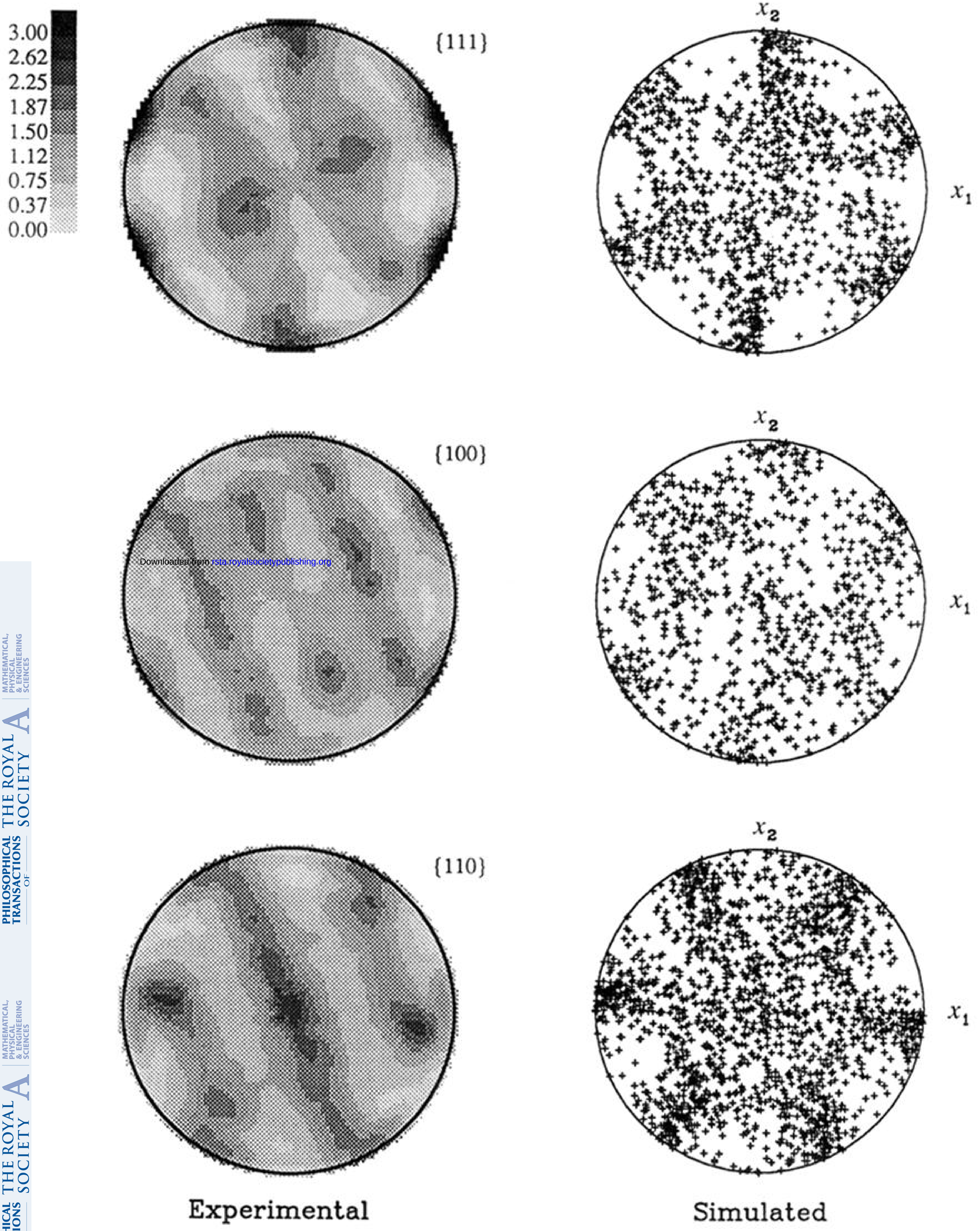

Figure 12 (*c*). Experimental and simulated crystallographic texture for planar simple shear to $\gamma_{12} = -0.75$.

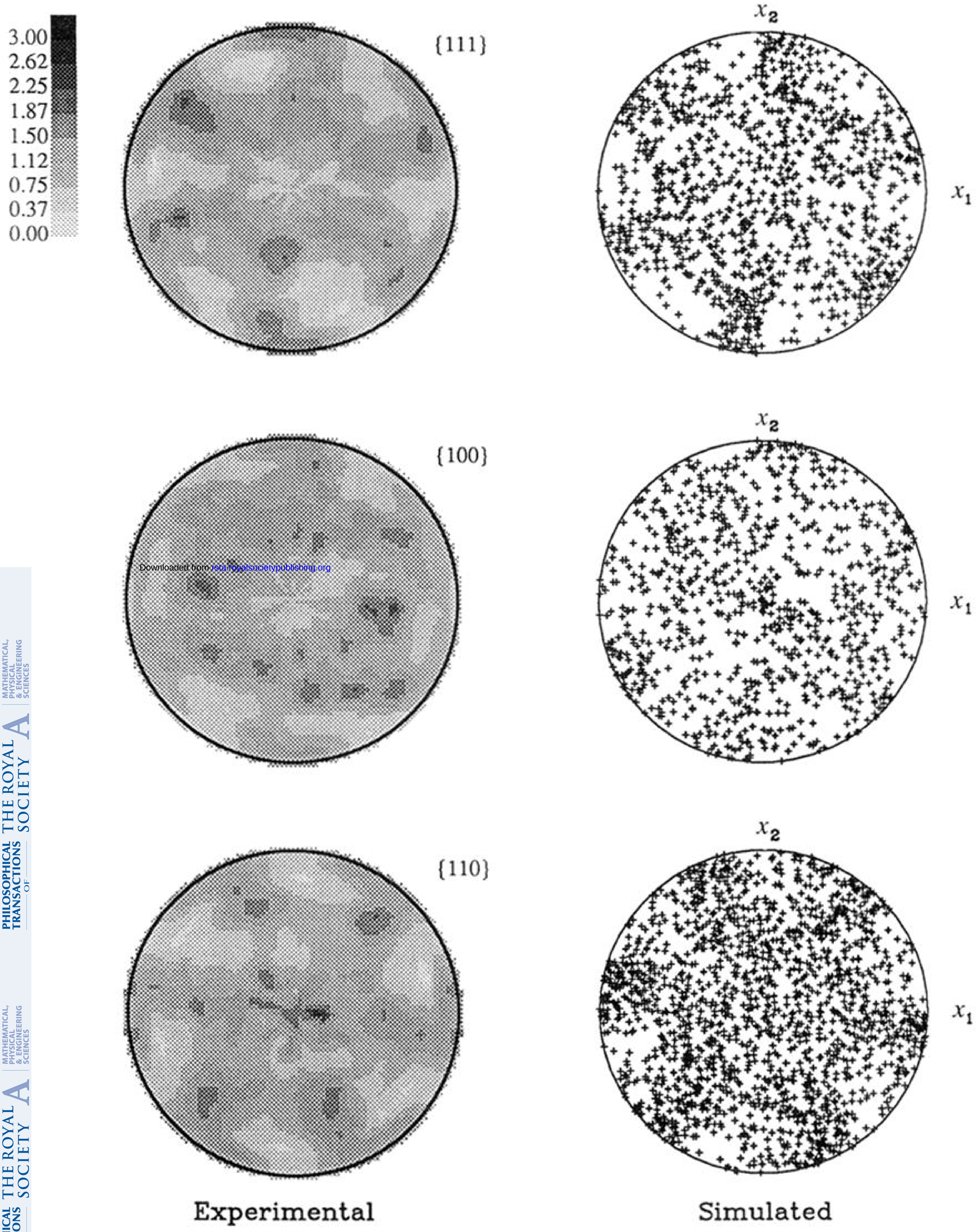

Figure 12 (*d*). Experimental and simulated crystallographic texture for planar simple shear to $\gamma_{12} = -1.16$.

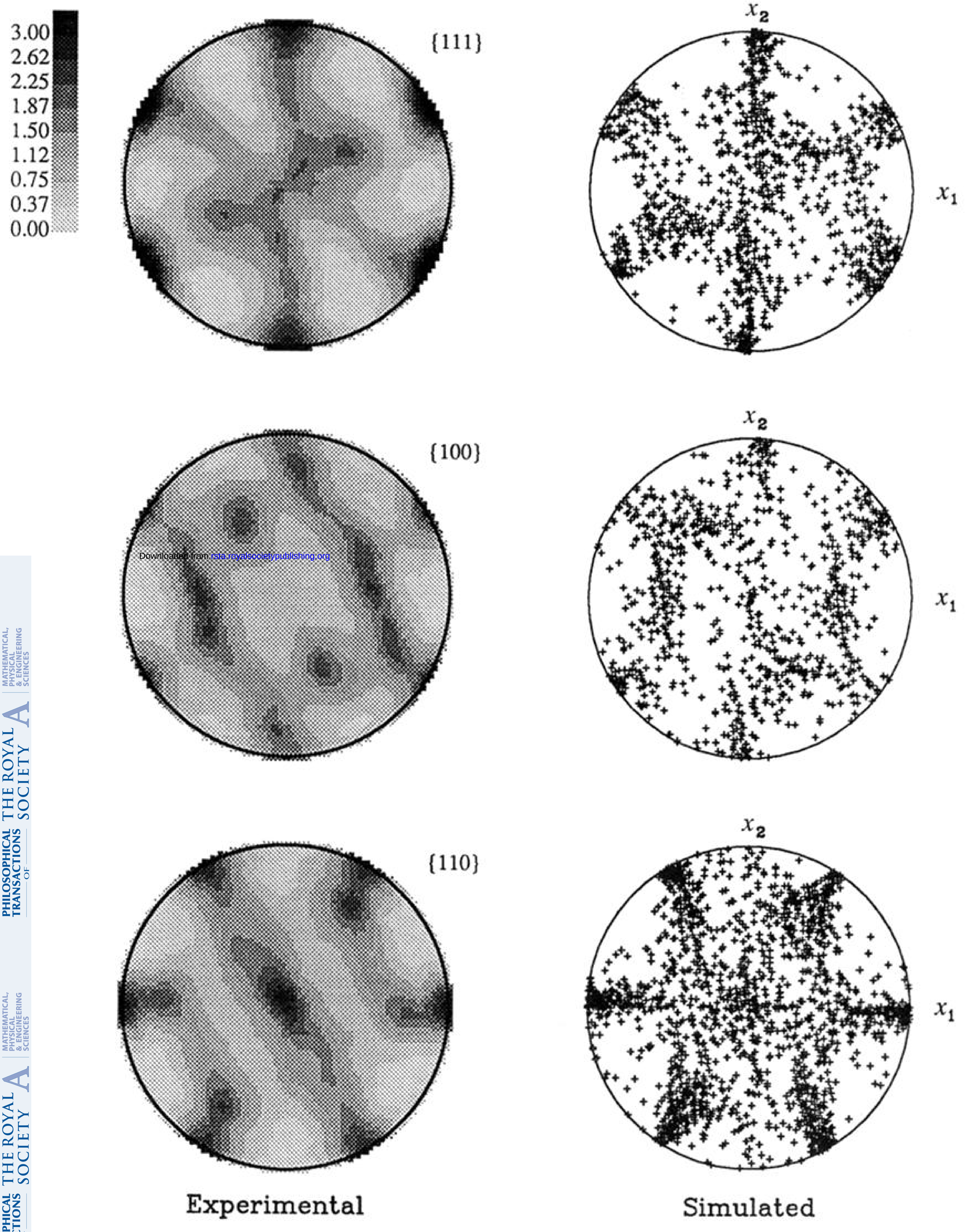

Experimental

Simulated

Figure 12(*e*). Experimental and simulated crystallographic texture for planar simple shear to $\gamma_{12} = -1.40$.

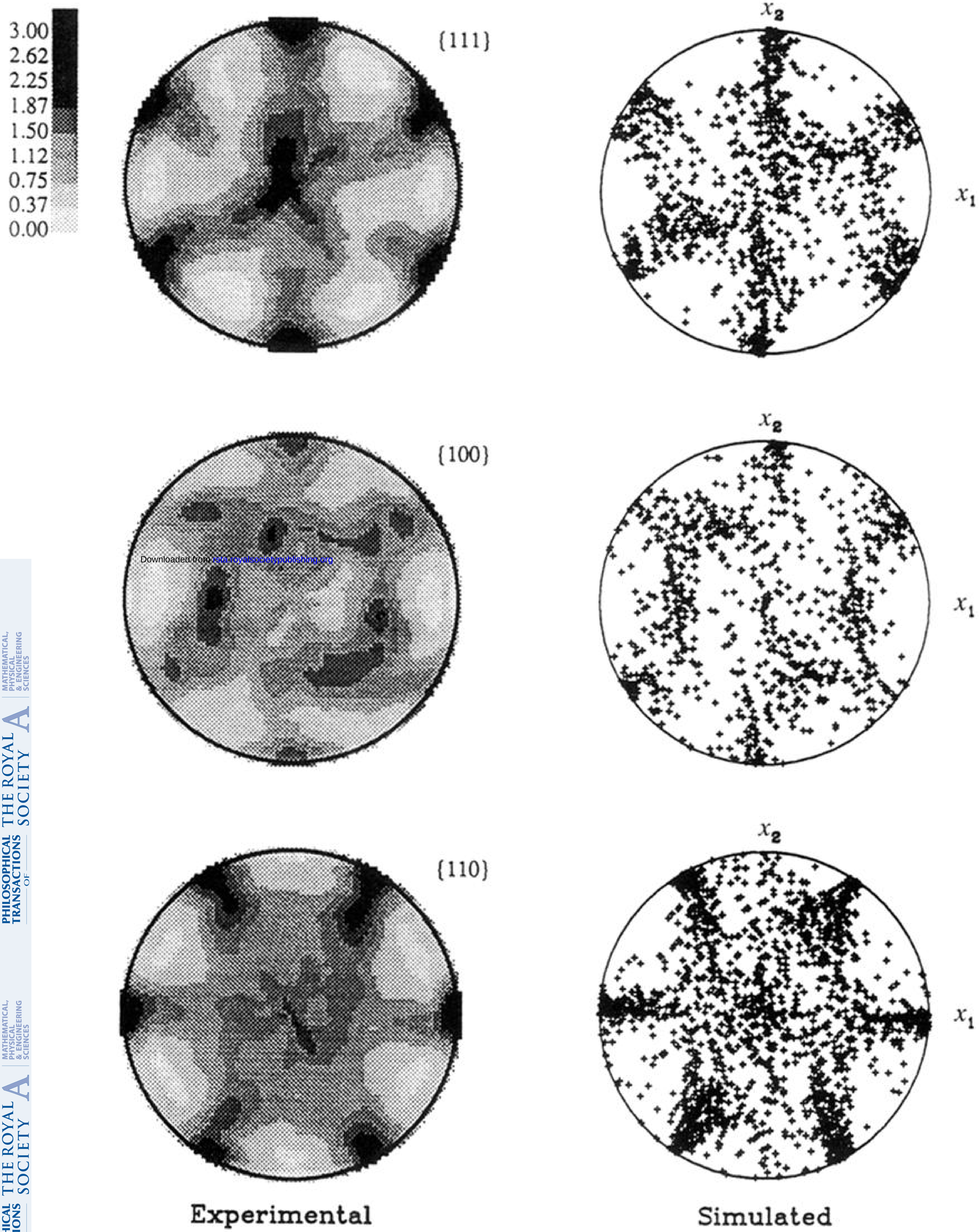

Figure 14. Experimental and simulated crystallographic texture for thin wall tube torsion to $\gamma_{12} = -1.50$.

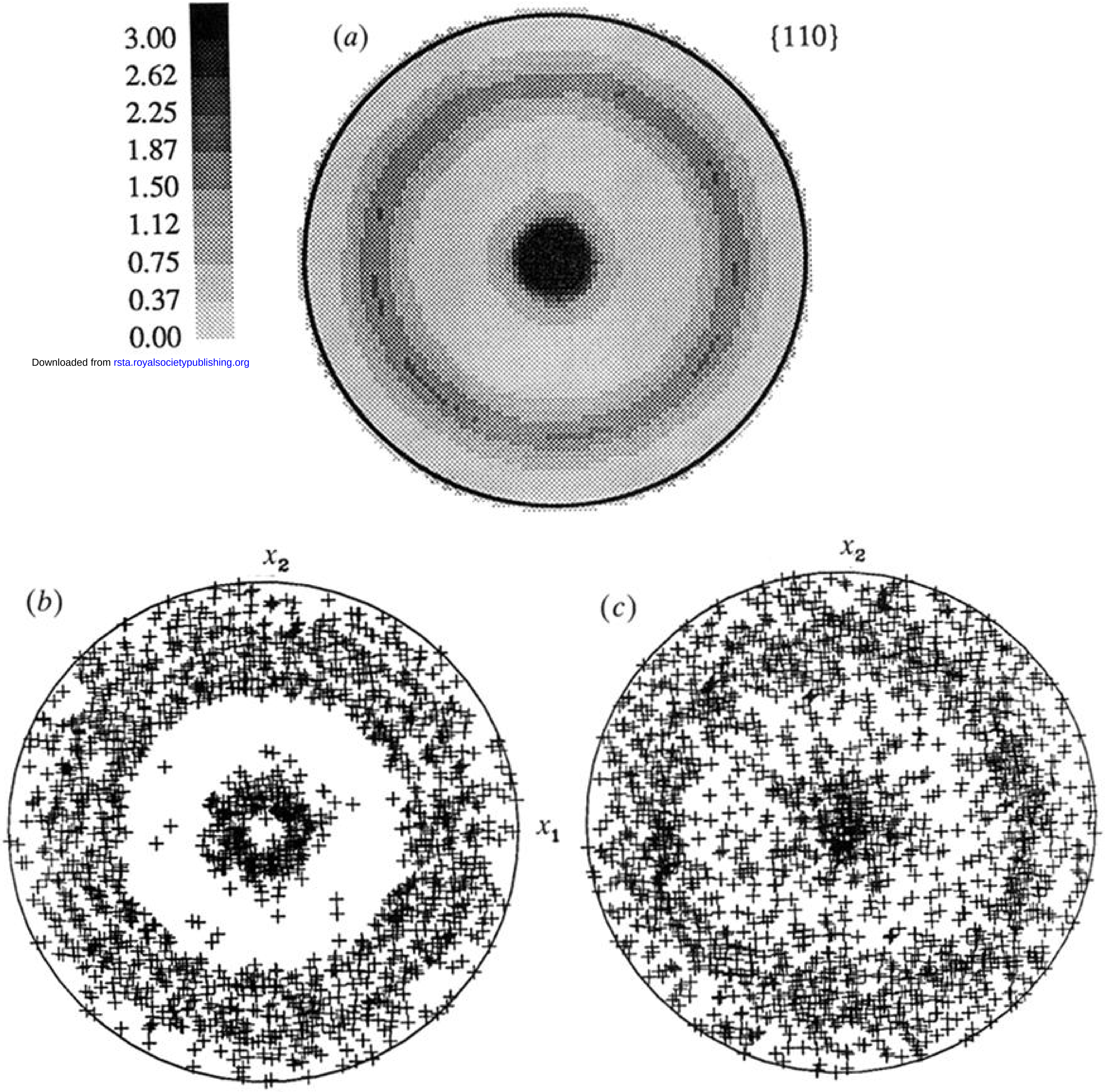

igure 16. {110} pole figures after compression to $\epsilon_{33} = -1.00$. (*a*) Experimental. (*b*) Taylor model lculation using crystals with the same initial orientations as those used for the finite element lculation. (*c*) Finite element calculation.

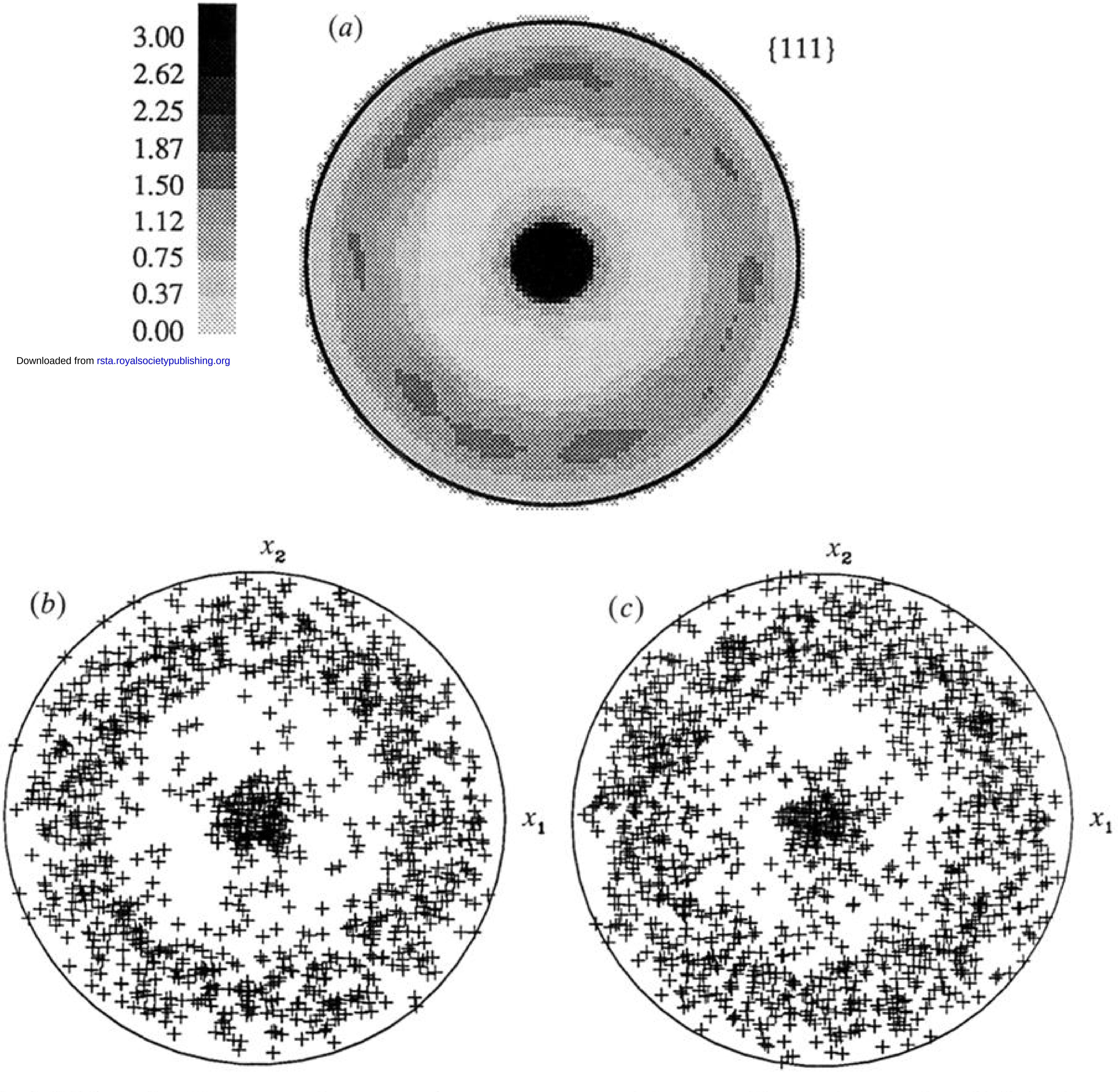

igure 17. {111} pole figures after tension to $\epsilon_{33} = 0.37$. (*a*) Experimental. (*b*) Taylor model lculation using crystals with the same initial orientations as those used for the finite element lculation. (*c*) Finite element calculation.

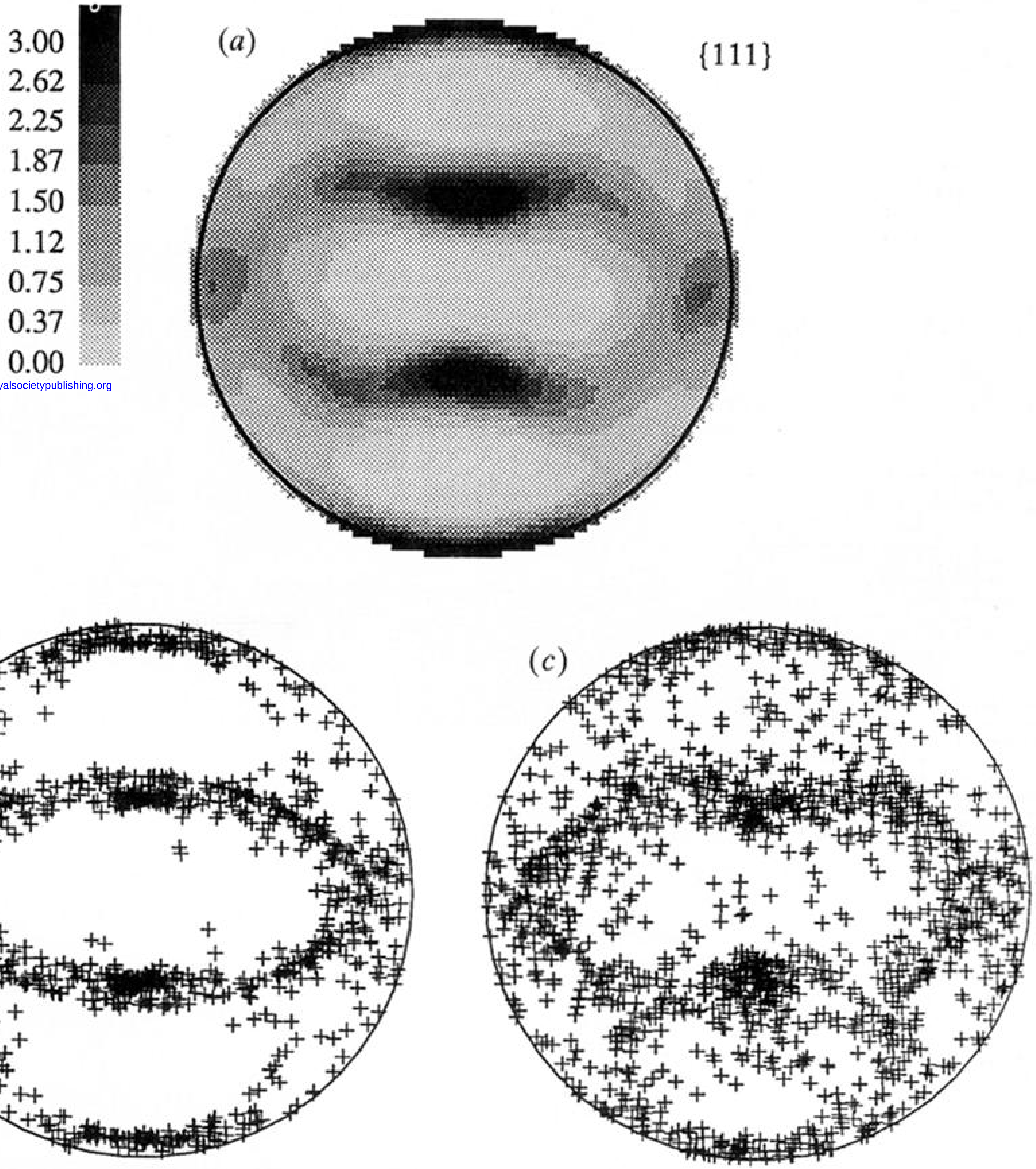

igure 20. {111} pole figures after plane strain compression to $\epsilon_{33} = -1.0$. (*a*) Experimental. (*b*) aylor model calculation using crystals with the same initial orientations as those used for the finite ement calculation. (*c*) Finite element calculation.

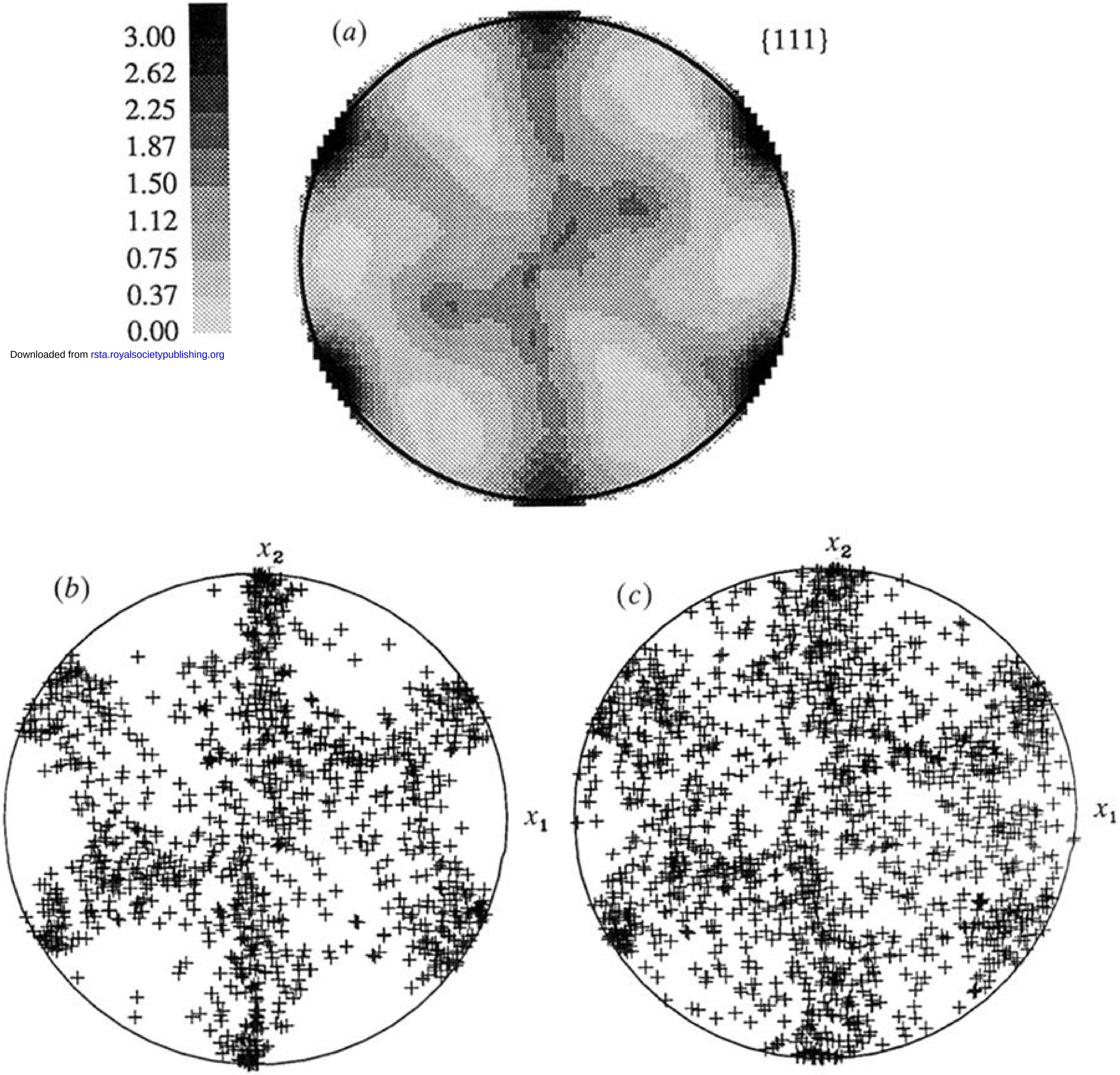

gure 22. {111} pole figures after simple shear to $\gamma = -1.4$. (*a*) Experimental. (*b*) Taylor model lculation using crystals with the same initial orientations as those used for the finite element lculation. (*c*) Finite element calculation.